The advective Brewer-Dobson circulation in the ERA5 reanalysis: variability and trends

Mohamadou Diallo[1], Manfred Ern[1], and Felix Ploeger[1,2]

[1]Institute of Energy and Climate Research, Stratosphere (IEK–7), Forschungszentrum Jülich, 52 425 Jülich, Germany.
[2]Institute for Atmospheric and Environmental Research, University of Wuppertal, Wuppertal, Germany.

Correspondence: Mohamadou Diallo (m.diallo@fz-juelich.de)

Abstract.

The stratospheric Brewer-Dobson circulation (BDC) is an important element of climate as it determines the transport and distributions of key radiatively active atmospheric trace gases, which affect the Earth's radiation budget and surface climate.

Here, we evaluate the inter-annual variability and trends of the BDC in the ERA5 reanalysis and inter-compare with the
5 ERA-Interim reanalysis for the 1979–2018 period. We also assess the modulation of the circulation by the Quasi-Biennial Oscillation (QBO) and the El Niño-Southern Oscillation (ENSO), and the forcings of the circulation by the planetary and gravity wave drag. A comparison of ERA5 and ERA-Interim reanalyses shows a very good agreement in the morphology of the BDC and in its structural modulations by the natural variability related to QBO and ENSO. Despite the good agreement in the spatial structure, there are substantial differences in the strength of the BDC and of the natural variability impacts on
10 the BDC between the two reanalyses, particularly in the upper troposphere and lower stratosphere (UTLS), and in the upper stratosphere. Throughout most regions of the stratosphere, the variability and trends of the advective BDC are stronger in the ERA5 reanalysis due to stronger planetary and gravity wave forcings, except in the UTLS below 20 km where the tropical upwelling is about 40 % weaker due to a weaker gravity wave forcings at the equatorial flank of the subtropical jet. In the extra-tropics, the large-scale downwelling is stronger in ERA5 than in ERA-Interim linked to significant differences in planetary and
15 gravity wave forcings. Analysis of the BDC trend shows a global acceleration of the annual mean residual circulation with an acceleration rate of about 1.5 % per decade at 70 hPa due to the long-term intensification in gravity and planetary wave breaking, consistent with observed and future climate model predicted BDC changes.

1 Introduction

As a key element of the Earth climate system, the stratospheric Brewer-Dobson circulation (e.g. BDC; Brewer, 1949; Butchart,
20 2014) has gain a lot of interest during these last decades because of its role in changing climate and weather prediction (WMO, 2018; Baldwin and Dunkerton, 2001). The BDC determines the transport and distributions of key stratospheric trace gases like

ozone, water vapor, and aerosol, which affect the Earth's radiation budget and surface climate (Forster and Shine, 1997; Riese et al., 2012). Changes in the distribution of these trace gases most effectively impact surface climate, in particular, if they occur in the upper troposphere and lower stratosphere (UTLS) region (Lacis et al., 1998). Expected changes in the BDC as predicted by climate models will impact the trace gas composition in the UTLS and, thus, may have crucial consequences for regional

5 and global climate.

The BDC is defined as a slow wave-driven circulation in which large-scale air masses ascent in the tropics, drift poleward in the mid-latitude stratosphere (e.g. surf zone), and then are transported downward in the extratropical regions (Brewer, 1949; Holton et al., 1995; Butchart, 2014). This mean meridional transport of air masses can be characterized by the stratospheric mean mass flux as given by the *stratospheric residual circulation* and by two-way exchange due to eddy mixing (Waugh

10 and Hall, 2002; Ray et al., 2010; Garny et al., 2014; Ploeger et al., 2015a; Miyazaki et al., 2016). The residual circulation represents an approximation of the diabatic or Lagrangian mean circulation as described in the Transformed Eulerian Mean framework (Andrews et al., 1987). The residual circulation can be separated into two branches: a deep branch driven by planetary waves and a shallow branch driven by synoptic and smaller-scale gravity waves (Plumb, 2002; Birner and Bönisch, 2011). In addition, Lin and Fu (2013) further separated the shallow branch into two sub-branches: the transition branch (at

15 pressure 100-70 hPa) and the shallow branch (at pressure 70-30 hPa). The two-way mixing term is defined as a quasi-horizontal stirring and irreversible displacement of large-scale air masses induced by breaking of large- and small-scales waves in the surf zone, and turbulent mixing (McIntyre and Palmer, 1984; Randel, 1993; Shuckburgh and Haynes, 2003).

Driven by breaking waves in the stratosphere (Haynes et al., 1991; Rosenlof and Holton, 1993; Newman and Nash, 2000; Plumb, 2002; Shepherd, 2007) and varying on seasonal to decadal timescales with strongest downwelling over the winter pole

20 (Bönisch et al., 2011), the stratospheric residual circulation is further modulated by natural variability, including the El Niño–Southern Oscillation (ENSO) (Randel et al., 2009; Diallo et al., 2018, 2019), the Quasi-Biennial Oscillation (QBO) (Baldwin et al., 2001; Ern et al., 2014), volcanic aerosols (Thompson and Solomon, 2009; Garfinkel et al., 2017; Diallo et al., 2017), increasing Greenhouse Gas (GHG) levels (Butchart et al., 2010) and Ozone Depletion Substances (Li et al., 2008; Polvani et al., 2018). The interannual variability of the residual circulation is mostly induced by two major modes of climate variability, the

25 QBO and the ENSO, which trigger a modulation of vertical transport in the stratosphere by affecting the temperature structure and thus the tropical upwelling and extratropical downwelling (Plumb and Bell, 1982; Trepte and Hitchman, 1992; Niwano et al., 2003; Punge et al., 2009). Future projections of climate models predict changes in the waves' propagation due to increasing GHG concentration levels (Shepherd and McLandress, 2011), which, in turn, alters the stratospheric residual circulation and its modulations by climate variability modes (Saravanan, 1990; van Oldenborgh et al., 2005; Latif and Keenlyside, 2009;

30 Cai et al., 2014; Kawatani and Hamilton, 2013).

Climate models predict that increasing GHG levels would globally strengthen the BDC (e.g., Butchart et al., 2010; Garny et al., 2011), consistent with negative temperature trends (Thompson and Solomon, 2005; Fu et al., 2019). This acceleration of the BDC results from the upward shift of the critical layer of wave breaking due to the strengthening upper flank of the subtropical jet (Shepherd and McLandress, 2011). Reanalyses estimates of mean age of stratospheric air (e.i. the average transit

35 time of air parcels through the stratosphere) show robust evidence for strengthening of the shallow branch and the southern

hemispheric deep branch of the BDC (e.g., Bönisch et al., 2011; Diallo et al., 2012; Monge-Sanz et al., 2012; Chabrillat et al., 2018; Ploeger et al., 2019), consistent with BDC trends derived from trace gas observations, including CO_2, SF_6 and N_2O (Stiller et al., 2012; Hegglin et al., 2014; Ray et al., 2010, 2014; Haenel et al., 2015). The southern deep branch is strongly modulated by the changes in ozone depletion (e.g. Lin and Fu, 2013; Polvani et al., 2018), therefore, its changes will

5   be affected by the ozone recovery. These findings are also consistent with the advective BDC trends found in reanalyses by Abalos et al. (2015). An updated time series of BDC changes since 1976 derived from in-situ observations of CO_2 and SF_6 in the northern hemisphere middle stratosphere (Engel et al., 2017) show no significant long-term BDC trend between 27 and 32 km, consistent with the mean age of air trends derived from the ERA-Interim and with some climate models (e.g., Garfinkel et al., 2017), but inconsistent with other known reanalyses (Chabrillat et al., 2018; Ploeger et al., 2019). Linz et al. (2017)

10 reported that many climate models are not yet able to reproduce the strength of the BDC as determined from observations. The fact that there is no clear observational evidence of northern hemispheric deep branch changes challenges both the validity of climate model predictions and observational uncertainties in the northern hemisphere middle stratosphere. According to Eichinger et al. (2019) notable source of uncertainty in reanalyses and for future climate projections lies in the strength of the BDC changes. Robust knowledge of the natural variability of the BDC on seasonal to decadal timescales, in turn, is a

15 prerequisite for the reliable detection and attribution of long-term anthropogenically-forced trends.

Commonly used as a basis for comparisons of the predicted BDC changes in climate models (Dietmüller et al., 2017; Polvani et al., 2018), the reanalysis data sets provide the best knowledge of the past and present atmospheric state by combining models with observations. Recently, the European Centre for Medium-Range Weather Forecasts (ECMWF) released its fifth generation of atmospheric reanalysis: the ERA5 global reanalysis (Hersbach et al., 2020). Built to replace the ERA-Interim reanalysis

20 (Dee et al., 2011), this newly available high-resolution reanalysis is expected to be a milestone for meteorological analysis as it includes improvements in the representation of atmospheric processes compared to the previous generations of reanalyses. Hence, it is of key importance to evaluate the representation and characteristics of the BDC in ERA5 reanalysis as well as its consistency with the ERA-Interim reanalysis.

In the present study, we seek to objectively evaluate the representation of the advective BDC in the ERA5 reanalysis in com-

25 parison with the ERA-Interim reanalysis, using different diagnostics, including the residual circulation transit time, the residual vertical velocity, the residual mass stream-function and its modulation by the QBO and ENSO signals (Butchart, 2014; Abalos et al., 2015; Ploeger et al., 2015b, a). We describe the reanalysis data sets and methods used in this study, including the Transformed Eulerian Mean and the statistical approaches, in Section 2. The mean climatology of the upwelling/downwelling mass flux and the inter-annual variability from the ERA5 reanalysis are discussed and compared with the ERA-Interim reanalysis

30 in Section 3.1. The residual stream-function and transit times are shown in Section 3.2. Section 3.3 presents the effects of different variability modes on the zonal mean wind, temperatures, residual vertical velocity and mass stream-function estimated using a statistical prediction model. Section 3.4 shows the modulation of the advective BDC by the planetary and gravity wave drag. Section 4 presents the trend in the advective BDC together with the trends in planetary and gravity wave drag. Finally, Section 5 provides further discussions and conclusions.

2 Data and Methodology

2.1 Description of the reanalyses

The wind and temperature data used in this study are from the ERA5 and the ERA-Interim reanalyses, provided by the ECMWF. The ERA5 reanalysis is based on the Integrated Forecasting System (IFS) and benefits from a decade of progress in model physics, dynamics, and data assimilation. Compared to ERA-Interim, ERA5 has better temporal resolution (6-hourly versus 1-hourly) and better horizontal (80 km versus 31 km) and vertical (60 levels versus 137 levels) resolutions and extends higher into the middle atmosphere (0.1 hPa versus 0.01 hPa or 65 km versus 80 km). The ERA5 has replaced the ERA-Interim reanalysis from 31 August 2019. Due to stratospheric temperature biases for 2000-2006 time period exhibited in the first version of ERA5, the ECMWF has published the ERA5.1 to improve upon the cold bias in the lower stratosphere seen in ERA5 (Simmons et al., 2020). In addition, a warm bias higher up persists for much of the period from 1979 (Hoffmann et al., 2019). Apart from higher spatial and temporal resolution, key improvements of ERA5 compared to ERA-Interim are better ability to resolve features like hurricanes and tropical cyclones, better representation of the tropospheric circulation; and assimilation of data from many recent satellite instruments (Li et al., 2020; Hoffmann et al., 2019). Potential limitations of reanalyses, including ERA5 and ERA-Interim, are non-physical trends and variability due to changes in the observing system such as the introduction of COSMIC radio occultation data in 2006, which affects the variability of temperatures near the tropical tropopause.

In this study, the wind and temperature fields from both reanalyses have been interpolated onto a $1° \times 1°$ longitude and latitude grid, and are extracted from the analysis available at 6 h interval. The difference between ERA-Interim and ERA5 is that the assimilation cycles start at 06:00 UT and 18:00 UT for ERA5 and at 00:00 UT and 12:00 UT for ERA-Interim. In addition, the dynamical fields in ERA5 are archived hourly as tendencies calculated over one hour, and no longer as accumulation over every 3 h hours as in ERA-Interim.

2.2 Metric of advective Brewer-Dobson circulation

Commonly used as a proxy for the advective BDC, the Transformed Eulerian Mean (TEM) residual circulation is derived from the standard formula of zonally-averaged zonal momentum equation, in latitude and log-pressure coordinates (ϕ, z), which is given by Andrews et al. (1987)

$$\frac{\partial \overline{u}}{\partial t} + \overline{v} \cdot \left[\frac{1}{a \cdot \cos\phi} \cdot \frac{\partial}{\partial \phi}(\overline{u} \cdot \cos\phi) - f \right] + \overline{w} \cdot \frac{\partial \overline{u}}{\partial z} = \overline{\mathfrak{S}} \tag{1}$$

where a is the Earth's radius, ϕ is latitude. $z = -H \cdot \ln(\frac{p}{p_s})$ is the the log-pressure height (vertical coordinate), H is a constant height defined as the scale height ($= R \cdot T_s/g$) for the log-pressure coordinate taken as 7 km, $T_s (= 240\,K)$ is chosen as standard reference temperature, R is the gas constant for dry air, $P_s (= 1013\,hPa)$ is chosen as standard reference pressure, (u, v, w) are respectively the zonal mean, meridional and vertical wind velocity, $\overline{\mathfrak{S}}$ corresponds to the total zonal momentum forcing and Ω is the Earth's rotation rate. The Coriolis frequency is $f = 2 \cdot \Omega \cdot \sin\phi$. Here, and in the following, the zonal and the deviations

from the zonal mean are respectively indicated by an over-bar and a prime. The partial derivative with respect to z (vertical) and ϕ (meridional) direction are indicated by $\frac{\partial}{\partial z}(.)$ and $\frac{\partial}{\partial \phi}(.)$ respectively.

As the advective BDC is a the Lagrangian mean circulation, the Eulerian mean velocity is not a sufficient and direct diagnostic metric. However, a useful proxy for the Lagrangian mean circulation under time-averaged conditions is provided by the
5   residual mean meridional circulation $(\overline{v^*}, \overline{w^*})$ (Andrews and McIntyre, 1976, 1978; Dunkerton et al., 1978; Holton, 1990). The latitudinal and vertical components of the residual mean meridional circulation $(\overline{v^*}, \overline{w^*})$ and the mean mass stream-function of the residual circulation, $\psi^*(\phi, z)$, are given as follows

$$\overline{v^*} = \overline{v} - \frac{1}{\rho_{sc}} \cdot \left(\frac{\rho_{sc} \cdot \overline{v' \cdot \theta'}}{\overline{\theta}_z} \right)_z = -\frac{1}{\rho_{sc} \cdot \cos \phi} \cdot \frac{\partial \psi^*}{\partial z} \tag{2}$$

$$\overline{w^*} = \overline{w} + \frac{1}{a \cos \phi} \cdot \left(\cos \phi \cdot \frac{\overline{v' \cdot \theta'}}{\overline{\theta}_z} \right)_\phi = \frac{1}{a \cdot \rho_{sc} \cdot \cos \phi} \cdot \frac{\partial \psi^*}{\partial \phi} \tag{3}$$

10   Introducing the equations (2, 3) into the equation (1) will lead to the TEM momentum equation (Andrews and McIntyre, 1978)

$$\frac{\partial \overline{u}}{\partial t} + \overline{v^*} \cdot \left[\frac{1}{a \cdot \cos \phi} \cdot \frac{\partial}{\partial \phi} (\overline{u} \cdot \cos \phi) - f \right] + \overline{w^*} \cdot \frac{\partial \overline{u}}{\partial z} = \overline{X}_{urGWD} + DF = \overline{\Im} \tag{4}$$

where $\overline{X}_{urGWD}$ is the residual mean nonconservative forcing unresolved by the model and DF is the normalised EP-flux divergence. The $\overline{X}_{urGWD}$ contribution consists of parameterized gravity wave drag and further imbalances of the reanalysis
15   momentum budget that are caused by the data assimilation system, and that can be interpreted as another contribution of unresolved gravity waves (e.g., Alexander and Rosenlof, 1996; McLandress et al., 2012; Ern et al., 2014). The density $\rho = \rho_o \cdot exp(-z/H)$ is the stratification of the atmosphere. θ is potential temperature (hence, $w = -(H/p) \cdot (dp/dt)$, where $p = p_o \cdot exp(-z/H)$ is the pressure). The Eliassen-Palm (EP) flux, $\mathbf{F}$, decreases exponentially with height due to the scaling factor $\rho_{sc} = \exp(-z/H) = \rho/\rho_o$. DF can be decomposed into resolved planetary ($\overline{X}_{PWD}$) and resolved gravity ($\overline{X}_{GWD}$) wave drags
20   and is written as following

$$DF = \frac{\nabla \cdot \mathbf{F}}{a \cdot \rho_{sc} \cdot \cos \phi} = \frac{1}{a \cdot \cos \phi} \cdot \frac{\partial}{\partial \phi} (F_\phi \cdot \cos \phi) + \frac{\partial F_z}{\partial z} = \overline{X}_{PWD} + \overline{X}_{GWD} \tag{5}$$

with $\mathbf{F} = \{F_\phi, F_z\}$ the EP-flux vector, with respective latitudinal and vertical components

$$F_\phi = a \cdot \rho_{sc} \cdot \cos \phi \cdot \left(\overline{u}_z \cdot \frac{\overline{v' \cdot \theta'}}{\overline{\theta}_z} - \overline{v' \cdot u'} \right) \tag{6}$$

$$F_z = a \cdot \rho_{sc} \cdot \cos \phi \cdot \left\{ \left[2 \cdot \Omega \cdot \sin \phi - \frac{1}{a \cdot \cos \phi} \cdot \frac{\partial}{\partial \phi} (\overline{u} \cdot \cos \phi) \right] \cdot \frac{\overline{v' \cdot \theta'}}{\overline{\theta}_z} - \overline{w' \cdot u'} \right\} \tag{7}$$

25   DF represents an important part of the forcings of the mean mass flux circulation from the dissipation of resolved planetary and gravity waves. DF can be decomposed into wave numbers ranging from 1 to 180 following previous studies (Ern et al.,

Atmospheric
Chemistry
and Physics

Discussions

2014; Alexander and Rosenlof, 1996). The resolved planetary wave drag, $\overline{X}_{PWD}$, is estimated as the integration over zonal wave numbers ranging between 1–20 in equation (5). The total gravity wave drag, $\overline{X}_{GWD}$, is the sum of the small contribution of explicitly resolved gravity waves with zonal wave numbers larger than 20 in equation (5), parameterized gravity wave drag and the momentum budget imbalances induced by data assimilation. In the reanalyses, the missing wave drag can be considered

5 equal to the unresolved wave drag by the ECMWF model grid, therefore, contributing to the gravity wave forcings in the momentum equation (eq. 4). Thus, the sum of this missing wave drag and the integrated model-resolved wave drag between the 21 and 180 zonal wave numbers gives the estimate of the total gravity wave drag (Alexander and Rosenlof, 1996). For additional details please see Ern et al. (2014, 2015, 2016).

If we consider that $\overline{X}_{urGW} \neq 0$ and $DF \neq 0$, representing the zonal forcing due the wave activity such as planetary and gravity

10 waves, then, to maintain the steady conditions, the BDC has to stay non-zero Andrews and McIntyre (1976, 1978); Eliassen and Palm (1961); Charney and Drazin (1961). Hence under this approximation, the circulation resulting from the wave forcings is the BDC. Further, the mass stream-function of the residual circulation, $\psi^*(\phi, z)$, is obtained by integrating vertically the total forcing term from the equation (4). In the steady cases and under the downward control principle (e.g. Haynes et al., 1991; Rosenlof and Holton, 1993; Garcia and Boville, 1994), it can be written as

15
$$\psi^*(\phi, z) = \int\limits_{z}^{\infty} \left\{ \frac{a^2 \cdot \rho_{sc} \cdot \cos^2 \phi}{\overline{m}_\phi} \left(DF + \overline{X}_{urGW} - \frac{\partial \overline{u}}{\partial t} \right) \right\}_{\phi = \phi(z')} dz' \tag{8}$$

where the angular momentum per unit mass is defined by $\overline{m}(\phi) = a \cdot \cos \phi \cdot (\overline{u} + a \cdot \Omega \cdot \cos \phi)$. At a line, where angular momentum is constant, the mass stream-function is integrated along a contour $\phi(z)$.

The tropical upwelling mass flux $\mathscr{F}$ is given by

$$\mathscr{F} = 2\pi \cdot a^2 \int\limits_{\phi_-}^{\phi_+} \rho_{sc} \cdot \overline{w^*} \cdot \cos \phi \cdot d\phi \tag{9}$$

20 This upward tropical mean mass flux, that is the mass per unit time, is integrated for the whole set of latitude circles where the vertical residual component is positive (i.e. $\overline{w^*} > 0$).

In addition to the mean mass flux and the residual mean mass stream-function diagnostics, we also calculated the residual circulation transit time (RCTT) using a two dimensional backward trajectory model driven by the residual mean meridional circulation ($\overline{v^*}$, $\overline{w^*}$). Used a metric of the advective BDC strength, the RCTT is defined as transit time of an air parcel that

25 is only advected by the residual circulation through the stratosphere. For additional details about the method of the RCTT estimates please see Ploeger et al. (2015b).

2.3 Statistical prediction model

For appropriately quantifying the QBO- and ENSO-induced variability in the advective BDC, different metrics of the circulation, including the temperature, zonal wind, $\overline{w^*}$ and $\overline{\psi^*}$ are analyzed using an established statistical prediction model. This

regression analysis model has been described in details and applied in our numerous previous studies (Diallo et al., 2012, 2017, 2018, 2019; Tao et al., 2019). The statistical model is based on the principle that the monthly zonal mean time-series of the BDC metrics can be decomposed into a sum of different contributions, including a linear trend, QBO, ENSO, seasonal cycle and a residual. For a given metric of the advective BDC strength, BDC_{metric} (herein U, T, $\overline{w^*}$, ψ^* and wave drags), at any latitude and altitude position in the stratosphere, the regression model can be written simply as following

$$BDC_{metric} = Trend + SeasonalCycle + QBO + ENSO + residual \qquad (10)$$

The estimated QBO and ENSO amplitude variations are normalized by the standard deviation of the QBO and ENSO predictors, which the QBO index at $50\,hPa$ and the Multivariate ENSO Index (Wolter and Timlin, 2011). The statistical prediction model estimates an uncertainty using a Student's t-test (Zwiers and von Storch, 1995; Friston et al., 2007). Note that the contributions of volcanic aerosol and solar cycle are voluntarily omitted for simplifying the description as these terms are not diagnosed in this study.

3   Climatological advective BDC and its modulations

3.1   Inter-annual variability of the Upwelling

Evaluating the large-scale ascent and descent of air mass flux is a prerequisite for disclosing possible biases in the morphology and strength of the advective BDC. Therefore, we compare the tropical upwelling and extratropical downwelling of the air mass flux from the ERA5 to the ERA-Interim using the residual vertical velocity ($\overline{w^*}$). Figure 1a–i show the annual mean and seasonal variations of the $\overline{w^*}$ estimated from the two reanalyses, together with the associated differences for the 1979-2018 time period. Overall, there is a remarkably good agreement between the two reanalyses in the main structure of tropical upwelling and extratropical downwelling derived from the annual and seasonal mean $\overline{w^*}$ climatology (Fig. 1a, b). However, substantial differences in the strength of the tropical upwelling and extratropical downwelling arise in three distinct regions of the stratosphere (Fig. 1c). In the tropical pipe region associated with large-scale upwelling (e.g., Neu and Plumb, 1999; Ray et al., 2014), the ERA5 reanalysis exhibits a weaker annual mean tropical upwelling in the UTLS, consistent with the well-known faster ERA-Interim tropical upwelling than observations (Dee et al., 2011; Seviour et al., 2011; Ploeger et al., 2012). In the mid-latitude surf zone region associated with strong large-scale stirring, and poleward and downward transport (e.g., McIntyre and Palmer, 1984), the ERA5 reanalysis also shows a weaker downwelling. Conversely in the polar vortex region, the ERA5 shows a stronger large-scale downwelling of the air mass than the ERA-Interim, suggesting a stronger advective BDC in ERA5. The maximum difference in the annual mean extratropical downwelling is about $0.5\,\mathrm{mm.s}^{-1}$ and occurs in the southern hemisphere. The residual velocity also exhibits seasonal variations in these three distinct regions of the stratosphere with even larger differences between the two reanalyses in the upper stratosphere above $30\,\mathrm{km}$ (Fig. 1d–i). As the strength of advective BDC varies seasonally between the hemispheres, these large differences in the $\overline{w^*}$ are displaced toward the winter hemisphere in the upper stratosphere with a maximum of about $1.5\,\mathrm{mm.s}^{-1}$. The reasons of these discrepancies in
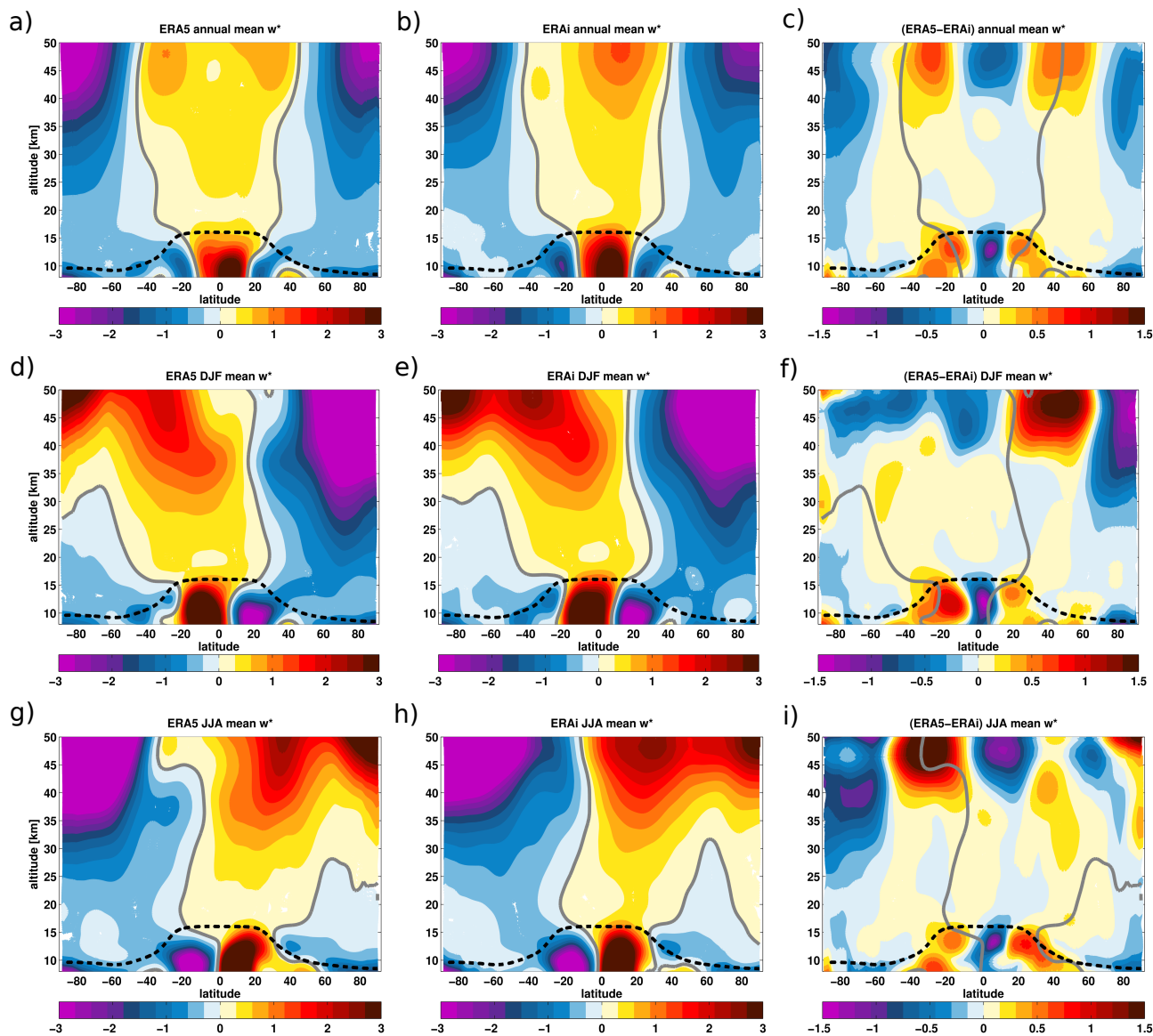
Figure 1. Annual and seasonal mean variations of the residual vertical velocity ($\overline{w^*}$) from the ERA5 (left) and the ERA-Interim (middle) together with the associated differences between the ERA5 and the ERA-Interim (right) for the 1979–2018 time period. The panels (**a–c**) show the annual mean climatology from the ERA5 (**a**), the ERA-Interim (**b**) and the associated differences (**c**). The panels (**d–f**) show the DJF mean from the ERA5 (**d**), the ERA-Interim (**e**) and its associated differences (**f**). The panels (**a–i**) show the JJA mean from the ERA5 (**g**), the ERA-Interim (**h**) and its associated differences (**i**). Grey vertical line indicates the zero $\overline{w^*}$ contours from the ERA5 and ERA-Interim, respectively. The climatological tropopause from the ERA-Interim is indicated as the llack dashed horizontal line. Unit: mm · s^{-1}.
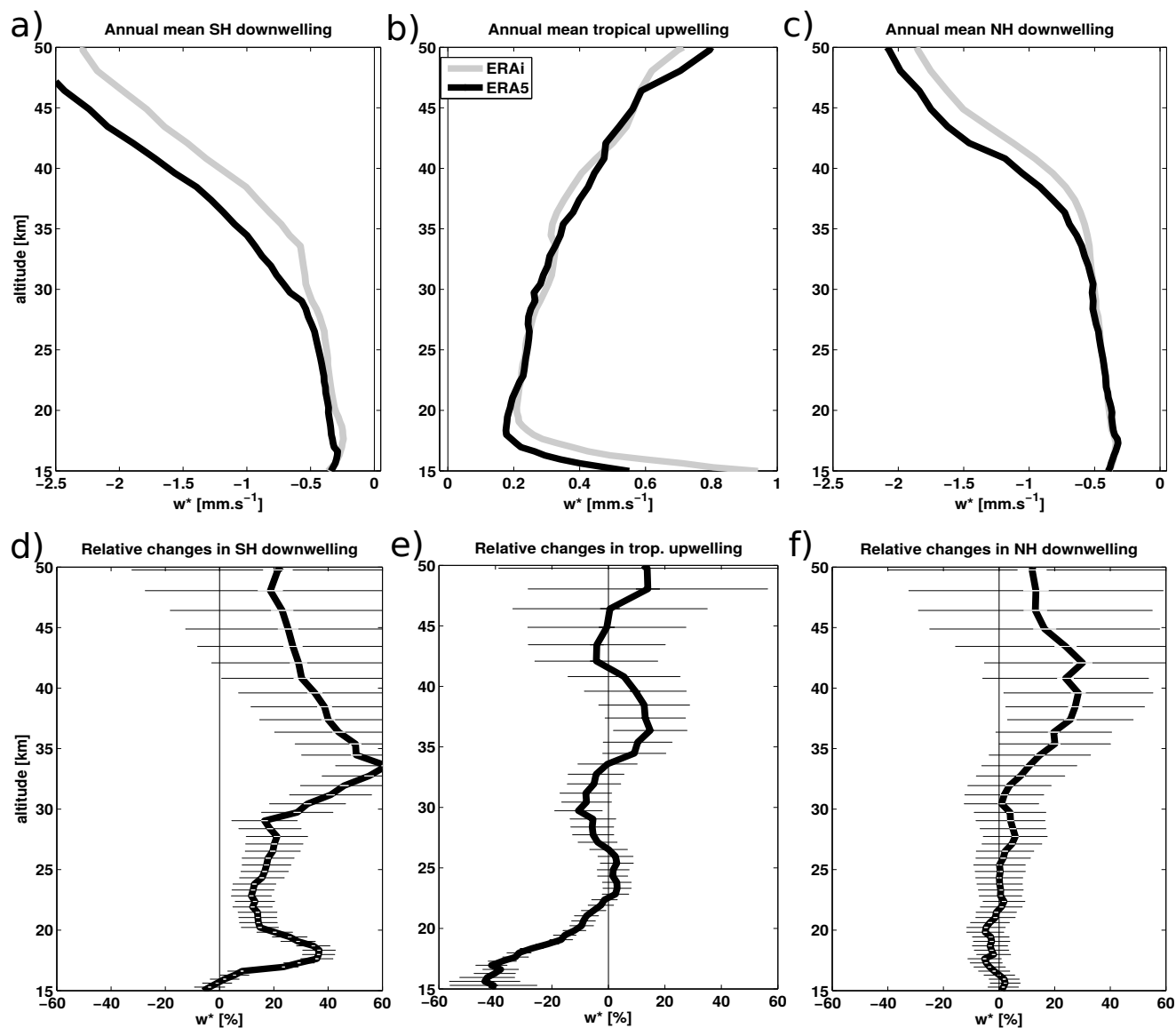
Figure 2. Vertical profiles of the annual mean $\overline{w^*}$ (in mm · s^{-1}) : (**a**) SH downwelling, (**b**) Tropical upwelling and (**c**) NH downwelling from the ERA5 (black) and the ERA-Interim (light-grey) for the 1979–2018 time period. Panels (**d**–**f**) show the relative differences of the $\overline{w^*}$ between the ERA5 and ERA-Interim in percent change relative to monthly mean. The error bars represent 15 times of the standard deviation from the mean differences.

tropical upwelling and extratropical downwelling are likely associated with the differences in wave forcings resulting from the improvements in the ERA5, including higher vertical and horizontal resolutions, higher model top, and new gravity wave parameterization scheme (Orr et al., 2010).
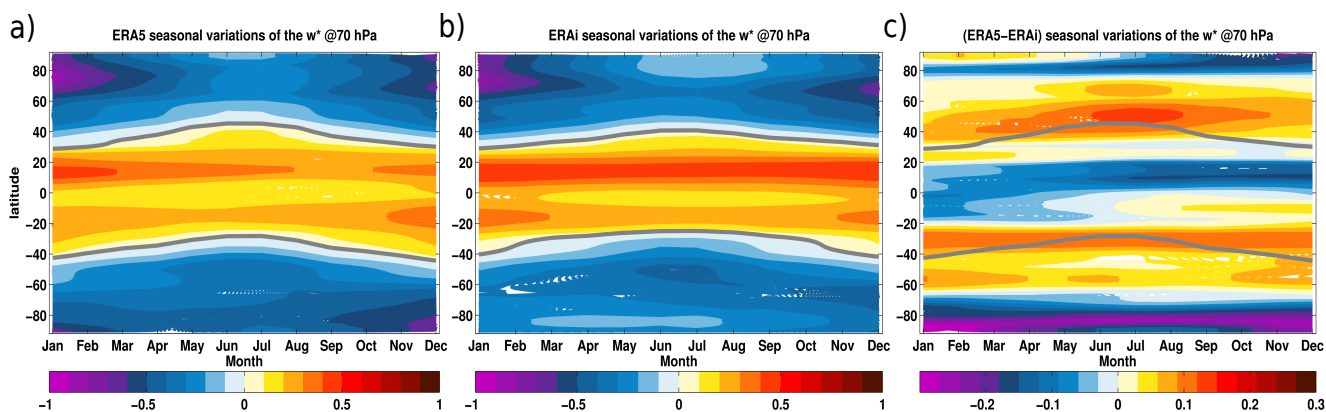
Figure 3. Monthly and latitudinal variations of monthly mean $\overline{w^*}$ at 70 hPa from the ERA5 (**a**), the ERA-Interim (**b**), and together with the difference between the ERA5 and the ERA-Interim (**c**) for the 1979–2018 period. Grey horizontal line indicates the zero $\overline{w^*}$ climatological from the ERA5 and ERA-Interim respectively. The unit of $\overline{w^*}$ is in mm . s^{-1}.

To quantify the differences in the air mass flux circulation between the two reanalyses, we average the annual mean $\overline{w^*}$ into vertical profiles based on the turnaround latitudes of tropical upwelling and extratropical downwelling together with the associated differences for the 1979–2018 period (Fig. 2 a–f). The vertical profiles of the $\overline{w^*}$ show a good agreement in the structure of the $\overline{w^*}$ between the two reanalyses for the 1979-2018 period (Fig. 2a–c). Despite the similarities in the vertical

5   structure, the relative differences in the $\overline{w^*}$ show a stronger large-scale downwelling in ERA5 than in ERA-Interim with a hemispheric asymmetry (Fig. 2 d–f). In the southern hemisphere, the large-scale downwelling is about 20 % stronger in ERA5 than in ERA-Interim below 30 km, and are even larger above with a maximum of about 60 % at 35 km (Fig. 2 c, f). In the tropics, the large-scale upwelling is about 40 % weaker in ERA5 than in ERA-Interim below 20 km (Fig. 2b, e), consistent with the stronger ERA-Interim upwelling (Fig. 1). Above 20 km, ERA5 reveals stronger tropical upwelling than ERA-Interim.

10   In the northern hemisphere, the downwelling differences between the two reanalyses are negligible below 30 km and reach 30 % above (Fig. 2c, f). The errorbars, which correspond to 15 times the standard deviation from the mean differences, indicate that the large differences in upwelling and downwelling correspond to the regions where the maximum variance occurs. The observed differences in the upwelling and downwelling are likely due to a combination of several factors, including a higher resolution, higher model top, new non-orographic gravity wave parameterization scheme, and the progress made in the more

15   realistic representation of the sponge layer in ERA5 and will be discussed later (Sect. 3.4).

The seasonal variations in the $\overline{w^*}$ and its associated differences between the two reanalyses are also assessed at 70 hPa for the 1979-2018 time period (Fig. 3a–c). The 70 hPa pressure level is commonly used as the reference level for model inter-comparisons of the upwelling strength of the air mass entering the stratosphere (e.g., Butchart et al., 2010). The tropical upwelling and extratropical downwelling patterns also agree remarkably well between the two reanalyses even in the variations

20   of the upwelling zero-line. The $\overline{w^*}$ exhibits a 6–month phase shift between the northern and the southern hemisphere mid-

latitudes, resulting from the correlation of the tropical upwelling annual cycle with the strongest descent located in the winter hemisphere (Fig. 3a, b). At 70 hPa, a seasonal variation of the differences in the $\overline{w^*}$ between the two reanalyses is also shown in Figure 3c. The weaker tropical upwelling in ERA5 varies seasonally between 0 and $20°$ N with a maximum of about $0.2 \, \mathrm{mm \cdot s^{-1}}$. In the mid-latitude, the large-scale downwelling is also weaker and varies seasonally with a maximum occurring

5   during the boreal summer (June-July-August). In the polar vortex region, ERA5 shows a stronger large-scale downwelling than ERA-Interim, as already evident from Fig. 1–2. The mass flux differences maximize in the polar vortex region of the southern hemisphere. These seasonal variations in the tropical upwelling and the extratropical downwelling results from the pumping action of the wave forcings (Dunkerton et al., 1981; Randel, 1993; Holton et al., 1995; Plumb and Eluszkiewicz, 1999).

3.2   Stratospheric residual circulation

10   In addition to the $\overline{w^*}$ analyses, we also evaluate the consistency and uncertainty in the residual circulation mass stream-function between the two reanalyses for the 1979-2018 time period. Figure 4a–i show a remarkably good agreement between the two reanalyses in the morphology of the advective BDC, regarding an ascent of air mass in the tropics, a motion in the stratosphere toward the mid- and high altitudes and latitudes, and descent into the mid- and high latitude regions. Note that apparent differences occur in the annual mean upwelling and downwelling circulation cells of the mass stream-function in the tropical

15   pipe, mid-latitude surf zone, and polar regions. Similarly to the $\overline{w^*}$, the residual circulation in ERA5 is weaker in the tropical pipe and the mid-latitude surf zone than in ERA-Interim, but stronger in the polar regions (Fig. 4a–c). The maximum difference in the residual circulation also occurs in the UTLS below 20 km, consistent with the $\overline{w^*}$ differences. The seasonal variations in the residual circulation also agree well in the structure, but not the strength during the winter and summer between the two reanalyses (Fig. 4d–i). During the boreal winter (December-January-February), the differences in the mass stream-function

20   between the two reanalyses are negative between the 0 and $20°$ N, which extends from the UTLS into the upper stratosphere. This negative difference indicates a weaker circulation in ERA5 and consistent with the weaker upwelling found in Fig. 3. However, the differences in the mass stream-function between the two reanalyses are positive between the $40°$ S and 0 and extend toward the southern hemisphere, leading to a stronger extratropical descent of the residual circulation in ERA5 than in ERA-Interim (Fig. 4d–f). The residual circulation is clearly stronger in ERA5 than in ERA-Interim. During the boreal summer

25   (June-July-August), these discrepancies in the residual circulation are reversed (Fig. 4e–i). These dominating seasonal features of the differences in the residual circulation suggest that the significant improvements in ERA5 likely induce a horizontal shift of upwelling in the UTLS compared to ERA-Interim.

For further insights into the circulation differences between the two reanalyses, we also evaluate the annual and seasonal mean variations of the residual circulation transit time (RCTT), which is defined as the integrated time-scale of air mass

30   transport by the pure residual circulation (e.g., Birner and Bönisch, 2011; Garny et al., 2014; Ploeger et al., 2015a, b). Note that the RCTT represents the integrated residual circulation effect, whereas the $\overline{w^*}$ is a local quantity. The RCTT shows a very good agreement in the morphology of the circulation between the ERA5 and ERA-Interim, e.g. the shorter transit time in the tropics (faster BDC) and longer transit time in the extra-tropics (slower BDC) for 2017-2018 period (Fig. 5a, b). However, the RCTT also shows clear differences in the residual circulation, consistent with the discrepancies in residual mass stream-
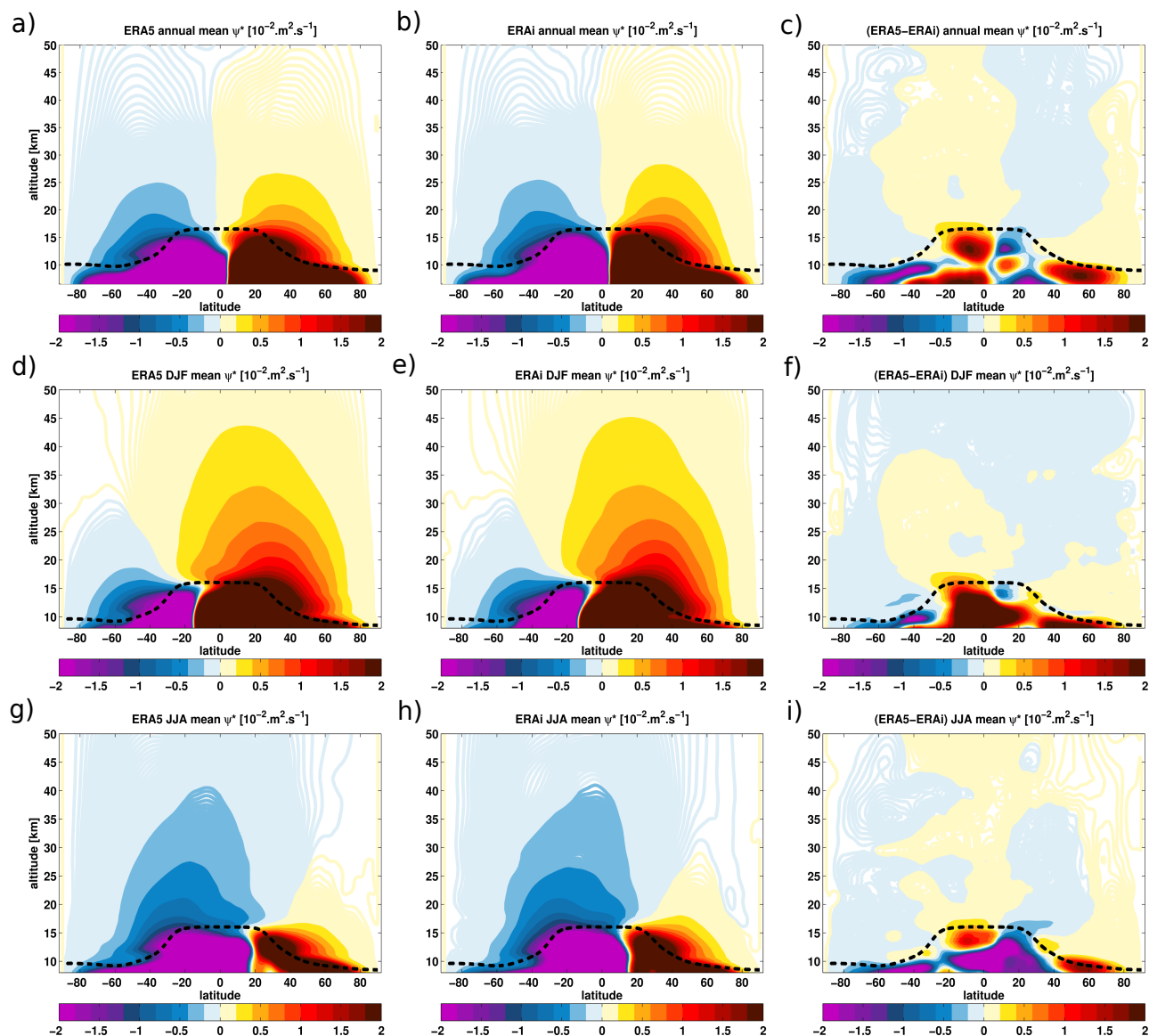
Figure 4. Zonal mean distribution of the annual and seasonal mean variations of the residual stream-function (ψ^*) from the ERA5 (left) and the ERA-Interim (middle) together with the associated differences between the ERA5 and the ERA-Interim (right) for the 1979–2018 time period. The panels (**a–c**) show the annual mean climatology from the ERA5 (**a**), the ERA-Interim (**b**) and the associated differences (**c**). The panels (**d–f**) show the winter season (DJF) mean from the ERA5 (**d**), the ERA-Interim (**e**) and its associated differences (**f**). The panels (**g–i**) show the summer season (JJA) mean from the ERA5 (**g**), the ERA-Interim (**h**) and its associated differences (**i**). The contours in the left and middle panels are spaced of about $0.005 \, \text{m}^2 \cdot \text{s}^{-1}$ and the contours in the right panel are spaced of about $0.0005 \, \text{m}^2 \cdot \text{s}^{-1}$. The climatological tropopause from the ERA-Interim is indicated as the black dashed horizontal line. The unit of ψ^* is in $\text{m}^2 \cdot \text{s}^{-1}$.
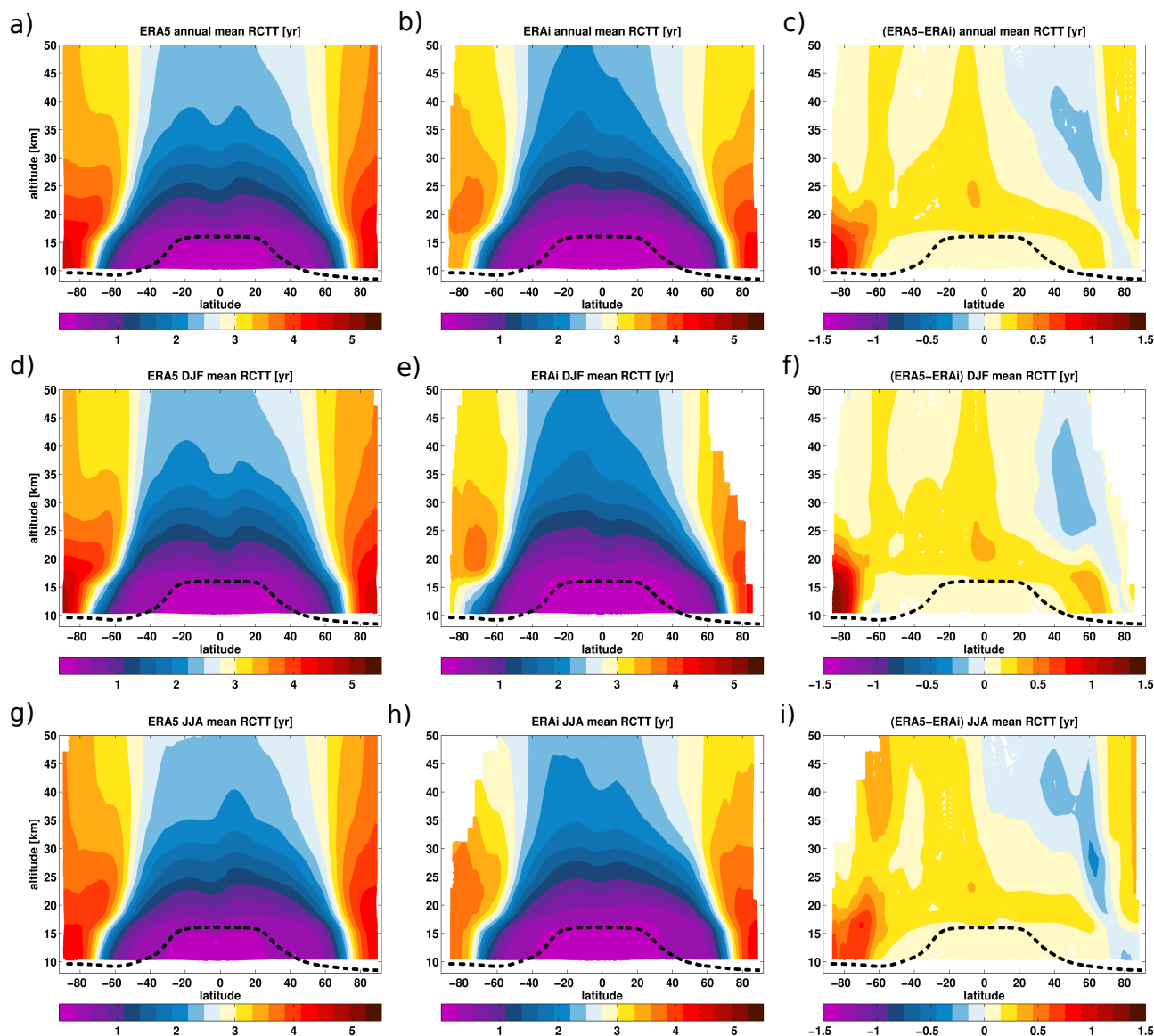
Figure 5. Zonal mean distribution of the annual mean and seasonal variations of the residual circulation transit time (RCTT) from the ERA5 (left) and the ERA-Interim (middle), together with the associated differences between the ERA5 and the ERA-Interim (right) for the 2017–2018 time period. The panels (**a**–**c**) show the annual mean climatology from the ERA5 (**a**), the ERA-Interim (**b**) and the associated differences (**c**). The panels (**d**–**f**) show the winter season (DJF) mean from the ERA5 (**d**), the ERA-Interim (**e**) and its associated differences (**f**). The panels (**g**–**i**) show the summer season (JJA) mean from the ERA5 (**g**), the ERA-Interim (**h**) and its associated differences (**i**). The climatological tropopause from the ERA-Interim is indicated as the black dashed horizontal line. The unit of RCTT is in yr.

function and residual vertical velocity previously discussed. In the tropical pipe (e.g., Neu and Plumb, 1999; Ray et al., 2014) and mid-latitude surf zone (e.g., McIntyre and Palmer, 1984), the annual mean RCTT in ERA5 exhibits longer transit time (below about 0.5 year) associated with the slower tropical ascent of the transition and shallow branch of the BDC (Lin and Fu, 2013; Diallo et al., 2019). In the northern hemisphere polar regions, the integrated residual circulation from the ERA5 shows

5   a shorter transit time (below about 0.5 year), consistent with a faster large-scale downwelling of the advective BDC in ERA5 than in ERA-Interim in the northern hemisphere. In the southern hemisphere, the residence time in ERA5 tends to be longer in ERA5 than in ERA-Interim. Notice that the RCTT is based just on a two year averaged, therefore, the circulation differences might not be representative of the full reanalysis period. However, the RCTT discrepancies are consistent with the differences in $\overline{w^*}$ and $\overline{\psi^*}$. This remark is even more relevant when analyzing the differences in the seasonal variations, which show almost

10   very similar differences as shown in the annual mean RCTT (Fig. 5d–i). The differences vary seasonally and the maximum difference is found in the southern hemisphere near the polar vortex (Fig. 5f, i).

3.3   Natural variability related to QBO and ENSO

To further understand the linkage of differences between the two reanalyses with the impact of natural modes of climate variability, we analyze the representation of the QBO and ENSO variability. One of the major mode of variability in the

15   ascending branch of the BDC on seasonal to intrannual is the QBO (Lindzen and Holton, 1968; Plumb and Bell, 1982). Composed of alternating westerly and easterly zonal wind shears, the QBO propagates downward from the tropical middle stratosphere into the troposphere with a period of ~ 28 months. Both reanalyses agree remarkably well in the downward propagating QBO phases (Fig. 6a, b). The depiction of the QBO westerly and easterly phases from the lower to the upper stratosphere (from about 15 to 50 km) in ERA5 is very similar to the ERA-Interim for the 1979–2018 time period. The QBO

20   disruption in January 2016, which was associated with the development of an easterly phase in the center of the westerly phase (Osprey et al., 2016; Newman et al., 2016), is clearly visible in both reanalyses. Apparent differences are also observed in the equatorial transitions in the eastward and westward zonal mean zonal wind and in the strength of QBO westerly and easterly phases between the ERA5 and ERA-Interim reanalyses. ERA5 exhibits stronger westerly and easterly shear of the QBO compared to the ERA-Interim (Fig. 6c). In addition to being stronger, the westerly QBO phase in ERA5 extends further

25   into the troposphere below the tropopause, while the ERA-Interim QBO westerly phase does not propagate that far downward. According to previous findings, the QBO westerly phase is sensitive to many model details, including the parametrized non-orographic gravity wave drag, and the vertical and horizontal resolution (Anstey et al., 2016; Geller et al., 2016; Polichtchouk et al., 2017, 2018; Shepherd et al., 2018). The amplitude of the westerly phase of the QBO and its frequency increase with increasing non-orographic gravity waves. In the ERA5 a non-orographic gravity wave drag parameterization is used, which

30   is different from the ERA-Interim, likely related to the observed differences (Orr et al., 2010; Scaife et al., 2002; Lott et al., 2012; Richter et al., 2014). In ERA-Interim, the Rayleigh drag used to be a substitute for the non-orographic gravity wave drag. When a Warner and McIntyre (2001) type scheme was introduced, this Rayleigh drag could be switched off. In addition, the finer vertical and horizontal resolution in ERA5 likely leads to better representation of the synoptic and small-scale waves
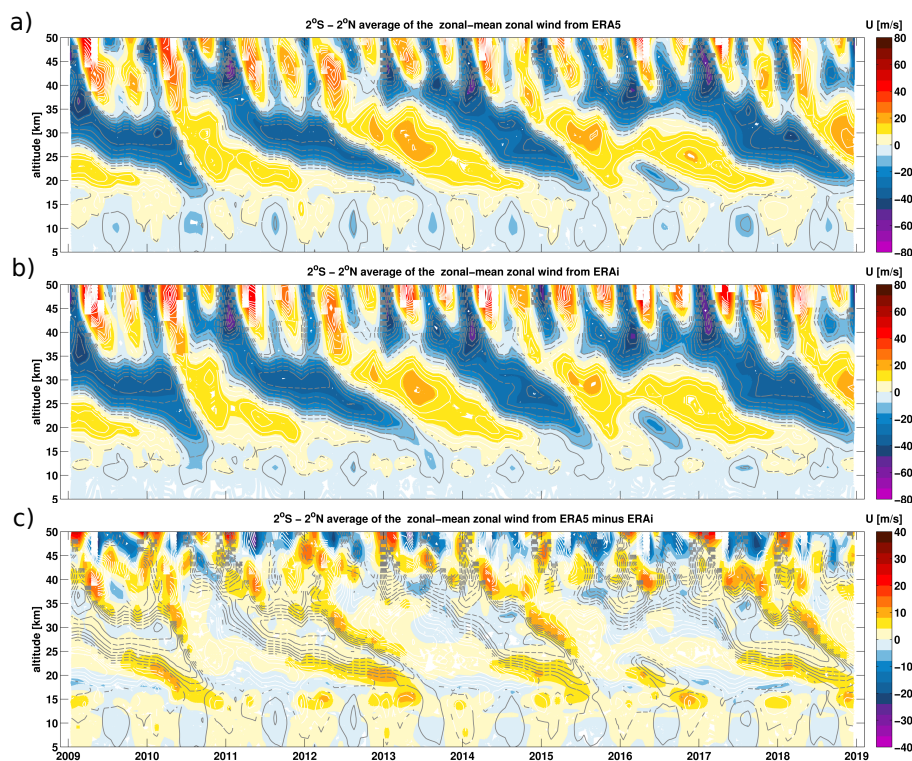
Figure 6. Tropical (2^oS to 2^oN average) zonal-mean zonal wind from the ERA5 (**a**), the ERA-Interim (**b**) and the difference between the ERA5 and the ERA-Interim (**c**) as a function of time and height. Unit: mm $\cdot$ s^{-1}.

as sources of gravity waves are better represented, such as convection, which is important for gravity wave driving the QBO (Lindzen and Fox-Rabinovitz, 1989).

Figure 7a–d shows the induced-QBO westerly and easterly amplitude variations in monthly mean zonal mean wind and temperatures estimated by fitting onto the QBO proxy with the statistical model (eq. 10) for the 1979–2018 time period. Both reanalyses agree very well in the phase and periodicity of the westerlies and easterlies. In addition to gravity waves, the QBO is partly driven by waves trapped in the equatorial region (Wallace et al., 1993; Baldwin et al., 2001; Ern and Preusse, 2009; Ern et al., 2014). The QBO modulates the stratospheric residual circulation in the meridional and vertical direction by affecting temperature and tropical upwelling (Plumb and Bell, 1982; Collimore et al., 2003; Niwano et al., 2003; Punge et al., 2009). The QBO westerly shear is partly induced by equatorially trapped Rossby-gravity waves and the QBO easterly shear is induced by Kelvin waves (Holton and Lindzen, 1972; Plumb, 1977). Figure 7a, b show that the QBO westerly amplitude variation occurs between 15 and 25 km, the QBO easterly amplitude variation between 25 and 35 km and again QBO westerly amplitude variation above 35 km. Note that the region of tropical westerly shear between 15 and 20 km is associated with anomalously warm tropical tropopause temperatures below 20 km (Fig. 7c, d) because it reduces the tropical upwelling and enhances the

15

horizontal transport and mixing of stratospheric trace gases poleward, consistent with anomalously cold temperature in the extratropical lower stratosphere (Plumb and Bell, 1982; Trepte and Hitchman, 1992). The strength of the QBO westerly wind and shear amplitude variations near the tropical tropopause region in ERA5 corroborates its weaker tropical upwelling in the UTLS compared to ERA-Interim (Figs. 1–3). Conversely, the region of tropical easterly shear between 20 and 30 km is

5   associated with anomalously cold tropical temperatures between 20 and 30 km, leading to enhanced tropical upwelling by the secondary meridional circulation associated with the QBO (Choi et al., 2002). The tropical upwelling is anti-correlated with the tropical temperature above the tropopause and its strength modulates trace gas mixing ratios by advecting tropospheric air into the stratosphere (Randel et al., 2006; Diallo et al., 2018; Ray et al., 2020). The strength of the QBO modulation of the circulation is stronger in ERA5 than in ERA-Interim as shown in both QBO-induced temperature and zonal mean wind

10 amplitude variations for the 1979–2018 period. Near the polar vortex region, the QBO effect on temperatures in ERA5 is larger than in ERA-Interim likely related to the Holton-Tan effect (e.i. the QBO modulates the Arctic polar vortex) (Holton and Tan, 1980; Garfinkel et al., 2012; Lu et al., 2014). In the upper stratosphere above 30 km, large differences in the strength are also visible in both temperatures and zonal mean winds associated with the differences in the QBO westerly shear and wind regions, consistent with the differences in $\overline{w^*}$ (Fig. 1).

15 In addition to the analysis of secondary meridional circulation, we analyzed the QBO- and ENSO-induced variability in the stratospheric residual circulation from variations in $\overline{w^*}$ and ψ^*. Considered as one of major modes of BDC modulation (Diallo et al., 2019), the coupled atmosphere-ocean phenomenon, ENSO, is defined as extreme sea surface temperature (SSTs) changes in the tropical Pacific Ocean. These drastic changes in SSTs encompass with severe surface climate and weather conditions (e.g., Bjerknes, 1969; Cagnazzo and Manzini, 2009; Wang et al., 2016). ENSO has two phases known as El Niño

20 (anomalously warm SSTs) and La Niña (anomalously cold SSTs), and its occurrence varies between 2 and 8 years (Philander, 1990; Baldwin and O'Sullivan, 1995). El Niño modulates the UTLS by warming the upper troposphere and cooling the tropical lower stratosphere. The latter has been associated with an acceleration of the ascending branch of the BDC (Randel et al., 2009; Calvo et al., 2010; Konopka et al., 2016).

To quantify the QBO- and ENSO-induced variability in the $\overline{w^*}$ and ψ^*, the statistical analysis (eq. 10) is performed by

25 explicitly including ENSO and QBO predictors to isolate their modulations of the BDC. The obtained QBO and ENSO amplitude variations are normalized by the standard deviation of the predictors' proxies for the 1979–2018 period, respectively. This direct approach gives similar results as the differentiating approach of the residuals (Diallo et al., 2017, 2018, 2019).

The results of the QBO-induced variability in the $\overline{w^*}$ show a very good agreement between the ERA5 and ERA-Interim reanalyses (Fig. 8a, b). Both reanalyses depict similar patterns of the QBO-induced changes in the $\overline{w^*}$. The structural changes

30 in $\overline{w^*}$ indicate a clear decrease in the tropical upwelling below 20 km induced by the QBO westerly shear between 15 and 20 km and consistent with QBO-induced anomalously warm tropical temperature changes in tropical UTLS below 20 km (Fig. 7c, d). Conversely, the tropical upwelling increases between 20 and 30 km due to the QBO easterly shear in that region, consistent with the QBO-induced anomalously cold tropical temperatures between 20 and 30 km (Fig. 3c, d). Another decrease in the tropical upwelling is induced by the QBO westerly shear above 30 km, consistent with the structure of QBO-induced temperature

35 changes (Fig. 7c, d). The $\overline{w^*}$ variations induced by the tropical QBO westerly shear region at altitudes 15-20 km, QBO easterly
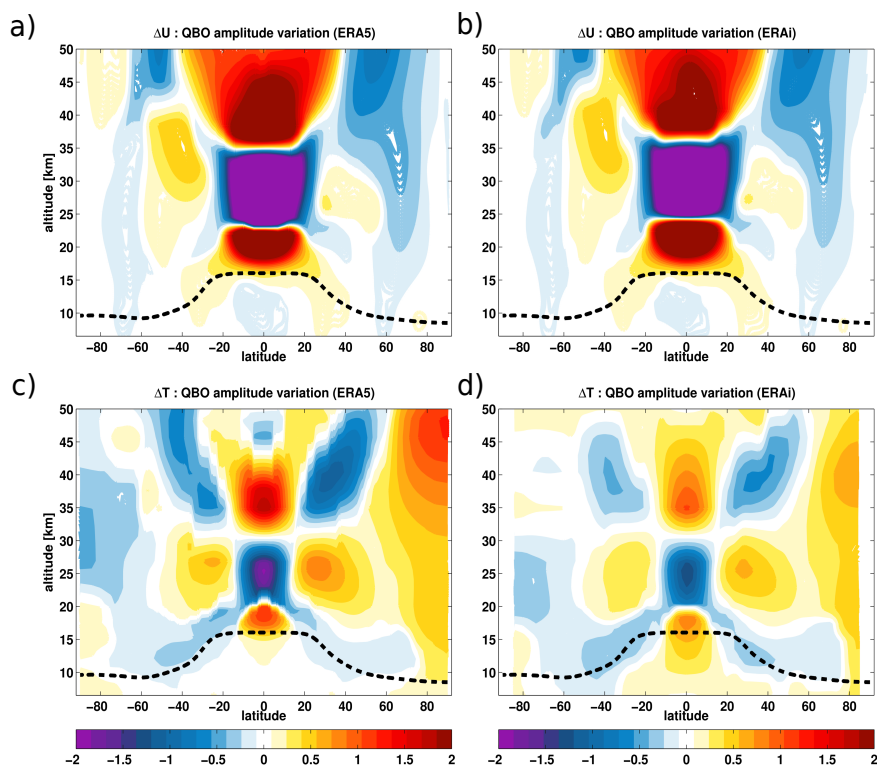
Figure 7. QBO amplitude variation derived from the ERA5 and the ERA-Interim zonal mean wind (**a**, **b**) and temperature (**c**, **d**) using the hybrid regression analysis for the 1979-2018 time period. The QBO amplitude variations are estimated by fitting on the QBO predictor using the regression model (10) The units of the QBO amplitude variations are $mm \cdot s^{-1}$ and K. In **a** and **b**, the easterly QBO shears and winds are in blue color, while the westerly QBO shears and winds are in red. The climatological tropopause from the ERA-Interim is shown in the black dashed horizontal line.

phase at altitudes 20-30 km and tropical westerly QBO shear above 30 km are consistent with previous findings regarding QBO modulations (Plumb and Bell, 1982; Trepte and Hitchman, 1992; Collimore et al., 2003; Niwano et al., 2003; Punge et al., 2009). Also note that the positive $\overline{w^*}$ anomalies induced by the QBO easterly shear in the tropical middle stratosphere below 30 km, and extending toward the extra-tropics are remarkably well captured in both reanalyses. The QBO westerly shear-induced negative $\overline{w^*}$ anomalies in the middle and upper stratosphere above 30 km agree fairly well in both reanalyses. The two main differences are the strength of the QBO-induced variability with the ERA-Interim, showing weaker region of QBO easterly and westerly effects. In addition, the positive $\overline{w^*}$ anomalies in the upper tropical stratosphere above 40 km are missing in the ERA-Interim.

Our analysis of the QBO-induced variability in the residual stream-function circulation is also consistent with the QBO impact on $\overline{w^*}$ (Fig. 8c, d). The QBO-induced morphological changes in the residual stream-function show a good agreement between the ERA5 and ERA-Interim. The region of QBO westerly shear decreases the residual circulation below the altitude of
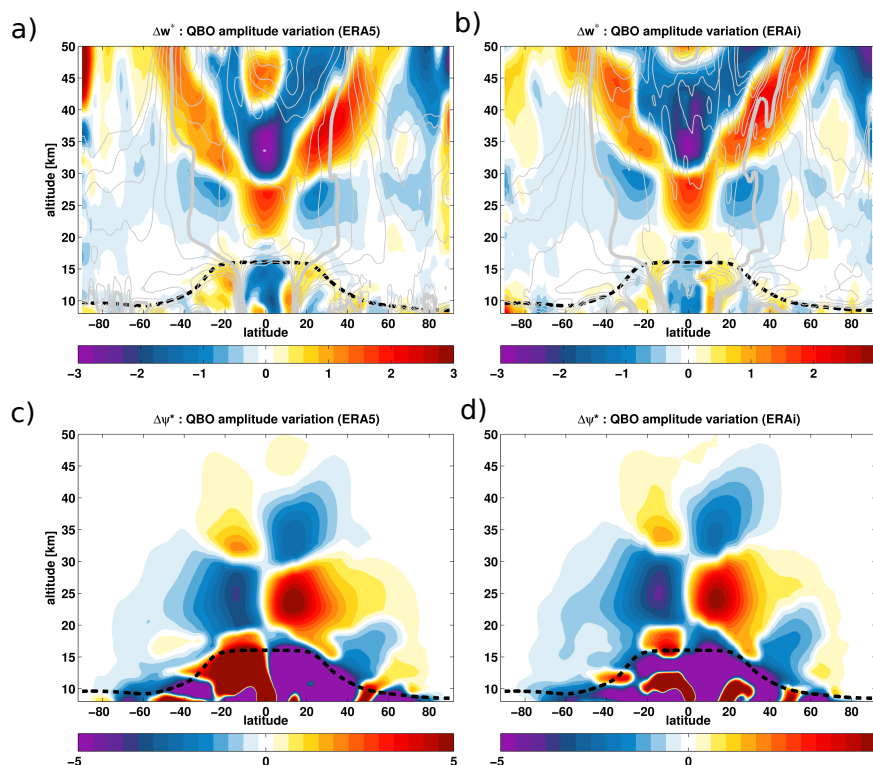
Figure 8. QBO impact on the residual vertical velocity ($\overline{w^*}$) (**a**, **b**) and the residual stream-function (ψ^*) (**c**, **d**) from the ERA5 (**a**, **c**) and the ERA-Interim (**b**, **d**) for the 1979–2018 period. The amplitude of the $\overline{w^*}$ and ψ^* variations attributed to the QBO signal are estimated by fitting on the QBO predictor using the regression model (10) and normalized by the standard deviation (SD) of the proxy for the 1979–2018 period. Unit: mm $\cdot$ s^{-1} $\times$ SD(proxy)). The climatological tropopause from the ERA-Interim is shown in the black dashed horizontal line. Zonal mean climatology of $\overline{w^*}$ is overplotted as dashed grey lines.

about 20 km. The regions of QBO easterly shear increases the residual circulation between the altitude of about 20 and 30 km while QBO westerly shear decreases it again above 30 km. The strongest QBO-induced changes in the residual circulation occur between the tropopause and at altitude of about 40 km with a maximum modulation of the circulation appearing between 20 and 30 km. Also, the residual stream-function shows a stronger QBO modulation in the ERA5 than in the ERA-Interim

5   (Fig. 8a, b).

The ENSO-induced variations in $\overline{w^*}$ agree well between the two reanalyses in their morphology. The structural changes in $\overline{w^*}$ in the UTLS region are characterized by positive anomalies in the tropics and negative anomalies in the extra-tropics (Fig 9a, b). The El Niño-like condition enhances the tropical upwelling between 15 and 20 km. These ENSO-induced variations in the $\overline{w^*}$ from the two reanalyses agree well. During El Niño-like condition, the strengthening of the tropical upwelling (positive

10   anomalies of the $\overline{w^*}$ in the tropics) increases upward transport of young air from the troposphere into the stratosphere (Calvo et al., 2010; Konopka et al., 2016; Diallo et al., 2019). The enhanced extratropical downwelling led to an increase in the
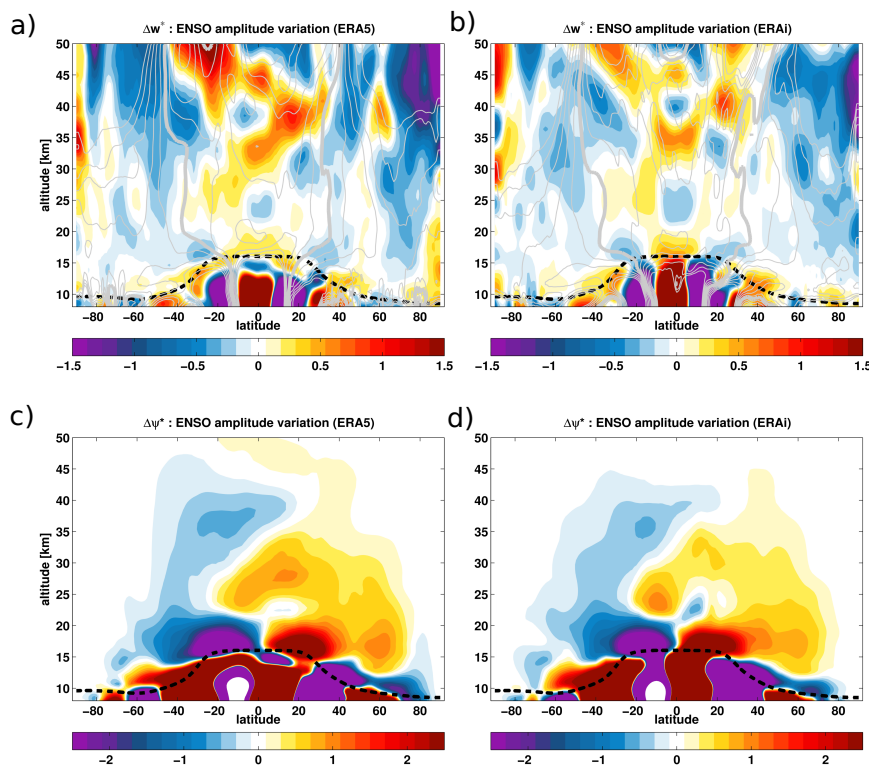
Figure 9. ENSO impact on the residual vertical velocity ($\overline{w^*}$) (**a**, **b**) and the residual stream-function (ψ^*) (**c**, **d**) from the ERA5 (**a**, **c**) and the ERA-Interim (**b**, **d**) for the 1979–2018 period. The amplitude of the $\overline{w^*}$ and ψ^* variations attributed to the ENSO signal are estimated by fitting on the ENSO predictor using the regression model (10) and normalized by the standard deviation of the proxy for the 1979–2018 period. Unit: mm · s^{-1} × SD(proxy)). The climatological tropopause from the ERA-Interim is indicated as the black dashed horizontal line. Zonal mean climatology of $\overline{w^*}$ is overplotted as dashed grey lines.

downward transport of old stratospheric air into the polar regions, competing with the projected acceleration of the BDC in a warming climate (e.g., McLandress and Shepherd, 2009; Lin and Fu, 2013; Butchart, 2014; Hardiman et al., 2014). However, there are differences in the magnitude of the ENSO-induced variation in $\overline{w^*}$. The $\overline{w^*}$ changes related to ENSO show a globally stronger tropical upwelling and extratropical downwelling in the ERA5 than in the ERA-Interim, except in the tropical UTLS below 20 km where ERA5 exhibits weaker anomalies than ERA-Interim. This specific difference in the UTLS suggests that because of the high vertical resolution in ERA5, the tropospheric ENSO-induced variation is more confined below the tropopause barrier in ERA5 than in ERA-Interim, consistent with larger inter-annual differences in the reanalyses at levels below the cold point (Tegtmeier et al., 2020). The ERA-Interim $\overline{w^*}$ positive anomalies in the inner tropics extend from the upper troposphere into the lower stratosphere while in ERA5 this is not visible. Additional differences occur in the tropical middle stratosphere between 20 and 30 km where ERA-Interim shows larger negative anomalies than the ERA5. In

the northern hemisphere upper stratosphere, ERA5 also reveals larger $\overline{w^*}$ negative anomalies than the ERA-Interim likely due to the difference in wave activities (Randel et al., 2002, 2008).

Insights on the ENSO-induced structural changes in the advective BDC become clearer from the analysis of the residual stream-function (Fig. 9c, d). The structural changes in the residual circulation induced by the ENSO also show a good agree-

5 ment between the ERA5 and ERA-Interim reanalyses, consistent with the $\overline{w^*}$ changes induced by the ENSO. In both reanalyses, ENSO strengthens the residual circulation of the BDC, particularly the shallow branch (Fig. 9c, d) (Diallo et al., 2019; Yang et al., 2014). The changes in the deep branch are less evident , but stronger in ERA5 than in ERA-Interim. This spatial changes in the residual circulation is consistent with positive (negative) stream function changes in the northern hemisphere (southern hemisphere). The apparent differences between the two reanalyses are associated with the strength of the ENSO-induced

10 acceleration of the BDC. In the inner tropical UTLS below 20 km, ERA5 exhibits weaker circulation anomalies than the ERA-Interim, consistent with the differences between the two reanalyses in the tropical upwelling (Fig. 9a, b). In the middle and upper stratosphere, the strengthening of the residual circulation is stronger in ERA5 than in ERA-Interim. The strengthening of the deep branch in response to ENSO does not extend as far upward in ERA-Interim as it does in ERA5, consistent with a less evident ENSO-induced changes in the deep BDC branch (Diallo et al., 2019). As all differences in the circulation and in

15 the natural variability point out to the possible discrepancies in the BDC forcings, we analyze the contribution of the planetary and gravity wave in the following (Sect. 3.4).

3.4 Planetary and gravity wave forcings

To better understand the contribution of wave forcings to the circulation and the natural variability differences between the ERA5 and ERA-Interim, we evaluate the net forcing, the planetary and the gravity wave driving the BDC. Figures 10a–i show

20 the annual mean climatology of the net forcings of the BDC and the contributions due to the planetary and gravity wave drag together with the associated differences between the ERA5 and ERA-Interim for the 1979–2018 time period. Note that the zonal wave forcing $\overline{\Im}$ can induce meridional wind contributions $\delta\overline{v^*}$. Assuming in the zonal momentum balance (eq. 4) steady state conditions ($\partial\overline{u}/\partial t = 0$) and negligible meridional and vertical gradients of the zonal wind, and assuming that the right hand side of equation (4) is only given by wave forcing $\overline{\Im}$, this equation reduces to $\overline{\Im} = -f * \overline{v^*}$. This means that the meridional wind

25 contribution $\delta\overline{v^*}$ that is attributed to zonal wave forcing can be written as: $\delta\overline{v^*} = -\overline{\Im}/f$. Correspondingly, positive wave drag indicating eastward forcing would weaken the BDC ($\delta\overline{v^*}$ is equatorward), and negative wave drag indicating westward forcing would weaken westerly winds, therefore, accelerating the BDC ($\delta\overline{v^*}$ is poleward). (Please note that the Coriolis parameter, f, changes its sign at the equator, and this will result in $\delta\overline{v^*}$ switching its sign at the equator if the sign of $\overline{\Im}$ does not switch).

Overall, the morphology of the mean wave drag climatology agrees well between the ERA5 and ERA-Interim, including

30 the positive wave drags in the easterly zonal mean wind regions and negative wave drag in the westerly zonal mean wind regions (Fig. 10a–f). However, significant differences occur in the amplitude of the wave drag (Fig. 10g–i). The gravity wave drag contributes the most to the UTLS differences in the net forcings of the BDC between the ERA5 and ERA-Interim, while the planetary and gravity wave contribution is stronger in the upper stratosphere (Fig. 10g–i). In the UTLS below 20 km, the previously reported weaker tropical upwelling in ERA5 compared to ERA-Interim is due to a weaker gravity wave breaking
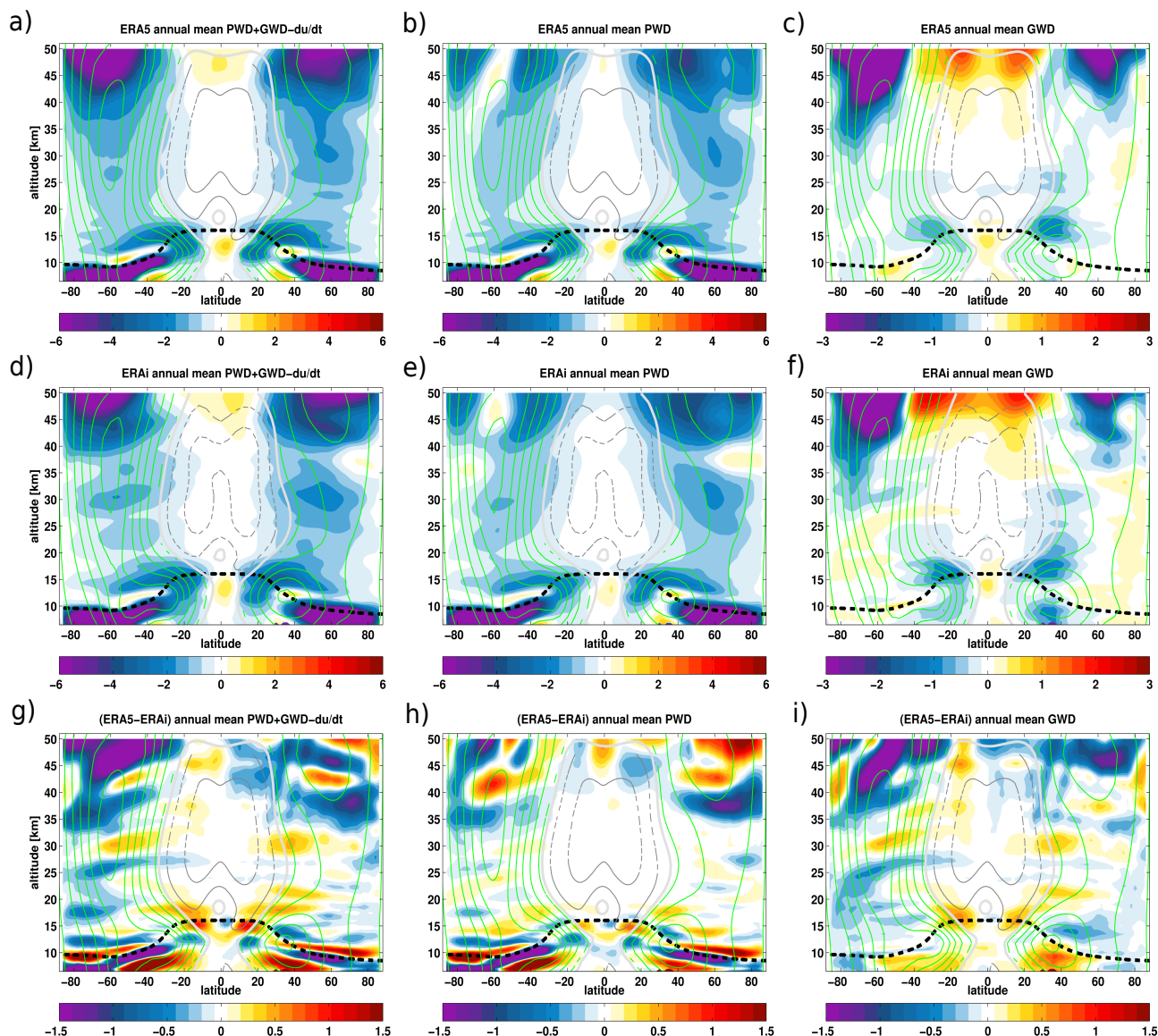
Figure 10. Zonal mean distribution of the annual mean net wave forcing (planetary wave drag + gravity wave drag - du/dt) (**a**, **d**), planetary wave drag (**b**, **e**) and gravity wave drag (**c**, **f**) together with the associated differences (**g-i**) between the ERA5 (**a–c**) and ERA-Interim (**d–f**) for the 1979–2018 time period. The unit of the wave drag is in $m \cdot s^{-1} \cdot day^{-1}$. The climatological tropopause from the ERA-Interim is indicated as the black dashed horizontal line. The thick white line indicates the zero line zonal mean wind. The thin green and grey lines indicate the climatological zonal mean wind.

at the equatorial flank of the subtropical jets in the ERA-Interim (Fig. 10g, i). The contribution of the planetary waves to the tropical upwelling differences is less evident. The breaking of synoptic and small-scale waves near the tropical tropopause

layer and the upper flank of the subtropical jets are the primary forcing sources of the transition and shallow branches of the BDC (Plumb, 2002; Shepherd and McLandress, 2011; Diallo et al., 2019). Thus, this difference in the strength of gravity wave breaking in the UTLS explains the weaker ERA5 tropical upwelling as observed in the residual vertical velocity, residual mass stream-function and the RCTTs. In the upper stratosphere above 30 km, the differences in the net forcings of the BDC

5   between the two reanalyses are also related to the contribution of the planetary and gravity wave breaking (Fig. 10g–i). While the planetary wave drag is stronger in the extra-tropics between 30 and 40 km in ERA5 than in ERA-Interim, it is weaker above 40 km. In the tropical upper stratosphere above 40 km, the gravity wave drag in ERA5 is significantly weaker than in ERA-Interim. These differences are likely due to better vertical and horizontal resolution, higher model top and changes to the non-orographic gravity wave drag parametrization scheme in ERA5 (Shepherd et al., 2018; Polichtchouk et al., 2018). In

10   ERA-Interim the non-orographic gravity wave drag was handled by the Rayleigh drag, but in ERA5 the scheme is based on non-orographic gravity waves parametrization from Warner and McIntyre (2001). So ERA5 does not have Rayleigh drag on any longer. The energy deposition from upward propagating gravity waves is a significant contributor to the thermodynamic budget at these altitudes. In addition, note that the sponge layer is also not always applied equally to different variables, and is sometimes enhanced in the vicinity of the equator presumably to control equatorial inertial instability.

15   Furthermore, the apparent differences in wave drag between the ERA5 and ERA-Interim reveal seasonal variations (Figs. A1a–i and A2a–i). During boreal winter, in the tropical UTLS region, the net wave forcings of the BDC in the ERA5 show a weaker gravity wave breaking at the equatorial flank of the subtropical jets than in ERA-Interim (Figs. A1g, i), leading to a weaker ERA5 tropical upwelling. Analogously to the annual mean of wave forcings of the BDC (Fig. 10), both planetary and gravity wave breaking contribute to the seasonal circulation differences between the ERA5 and ERA-Interim in the

20   upper stratosphere above 30 km. These circulation discrepancies in the upper stratosphere are even stronger during the boreal winter in the northern hemisphere. The net wave forcings of the BDC reveal that the planetary and gravity wave breaking are significantly stronger in the northern hemisphere during the boreal winter, suggesting a stronger deep branch of the BDC in ERA5 than in ERA-Interim, which is, in turn, consistent with the reported stronger large-scale downwelling in polar regions (Fig. A1h, i). During boreal summer, the differences in the tropical UTLS and upper stratosphere induced by mainly planetary

25   and gravity wave dissipation are also consistent with the discrepancies in the BDC between the ERA5 and ERA-Interim. In the UTLS region, the gravity wave breaking at the equatorial flank of the subtropical jet causes the differences between the ERA5 and ERA-Interim tropical upwelling (Fig. A2a–i). The observed maximum of the seasonal variations in the tropical upwelling at 70 hPa between 0 and 20° N is due to a weaker gravity wave breaking in the ERA5 UTLS. In the upper stratosphere, the gravity wave breaking in the southern hemisphere winter has a stronger contribution than the planetary waves and is also stronger

30   in ERA5 than in ERA-Interim, suggesting a stronger southern hemispheric deep branch (Fig. A2g–i). This is also consistent with the reported hemispheric asymmetry in the $\overline{w^*}$, RCTT, and natural variability induced variations. As the strength of the BDC trends is also driven by the net wave breaking, we expect the BDC trends to be impacted by the stronger wave drag in the ERA5 reanalysis, there, we estimate the trends in the following (Sect. 4).

4 Advective BDC trends

For better insights in the impact of stronger gravity and planetary wave drag on the BDC in ERA5, we also investigate the structural changes in the advective BDC and wave drag for the 1979–2018 time period (Fig. 11a–d). The ERA5 reanalysis shows an acceleration of the BDC, consistent with previous reanalysis studies (Diallo et al., 2012; Abalos et al., 2015; Miyazaki

5 et al., 2016) and climate model projections (e.g., Butchart et al., 2010; Hardiman et al., 2014). The annual mean trend of the residual circulation mass stream-function shows a quasi-global positive trend, indicating a strengthening of the shallow and deep branches of the BDC in both hemispheres (Fig. 11a). The negative BDC trend in the inner tropical UTLS suggests a weakening of the transition branch probably linked to the stratospheric shrinking (Šácha et al., 2019). The decomposition of the wave drag into planetary and gravity wave forcing trends led to an estimate of the impact of these two wave forcings on

10 the structural changes in the transition, shallow and deep branches of the BDC. The BDC trend in ERA5 is induced by the combined contribution of the gravity and planetary wave breaking (Fig. 11c, d). The negative trends in the net wave forcings of the BDC between 35 and 45 km indicate an intensified planetary and gravity wave breaking in both hemispheres (Fig. 10b– c). While the shallow branch is accelerated by enhanced gravity wave breaking in the tropical and subtropical UTLS region, the deep branch is driven by a sum of the contribution from the planetary and gravity wave breaking at high altitudes. The

15 planetary waves breaking seems to contribute the most to the acceleration of the deep branch of the BDC, consistent with previous studies (Sigmond and Shepherd, 2014; Abalos et al., 2015; Eichinger et al., 2020). The hemispheric asymmetry in the BDC trends is due to the asymmetry in wave breaking, which is stronger in the northern hemisphere than in the southern hemisphere as indicated by the negative net forcing trend (Fig. 11b). We also note that the southern hemispheric circulation cell exhibits an apparent structural difference compared to the northern hemispheric circulation cell. The southern hemisphere

20 residual circulation trend is weaker than in the northern hemisphere, consistent with the asymmetry in wave breaking trends, which are stronger in the northern hemisphere. A detailed analysis of the BDC trends will be presented in further studies using the stratospheric age of air and age spectrum. Note that the ERA-Interim still shows a negative trend in the residual stream-function (not shown), consistent with the weakening upwelling trend estimated from $\overline{w^*}$ (Seviour et al., 2011).

In addition, the time series of deseasonalized monthly mean tropical upwelling mass flux averaged between the turnaround

25 latitudes show a comparable inter-annual variability between the ERA5 and ERA-Interim reanalyses at the pressure level of 70 hPa (Fig. 12). The estimated annual mean upwelling mass flux is about 6.17×10^9 kg $\cdot$ s^{-1} for ERA5 and about 6.86×10^9 kg $\cdot$ s^{-1} for ERA-Interim for the 1979–2018 period, consistent with the multi-model mean value of 5.9 $\times 10^9$ kg $\cdot$ s^{-1} from previous studies (e.g, Butchart et al., 2010; Hardiman et al., 2014; Linz et al., 2017). The ERA5 tropical upwelling mass flux trend at 70 hPa calculated from $\overline{w^*}$ is about 1.5 % per decade, consistent with the observed BDC changes

30 of about 1.7 % per decade (Fu et al., 2019) and climate model predictions of an increase in the strength of the BDC of about 2 % per decade due to the increasing GHGs in the atmosphere (Butchart et al., 2010; Garny et al., 2011; Hardiman et al., 2014). While the climate model projected trend is statistically significant, th mass flux trend in ERA5 is not significant. Note that the reported negative long-term trend by Seviour et al. (2011) in the tropical upwelling mass flux estimated from the ERA-Interim $\overline{w^*}$ disappears in ERA5. This negative long-term trend in standard $\overline{w^*}$ calculations is found to be intricately related to
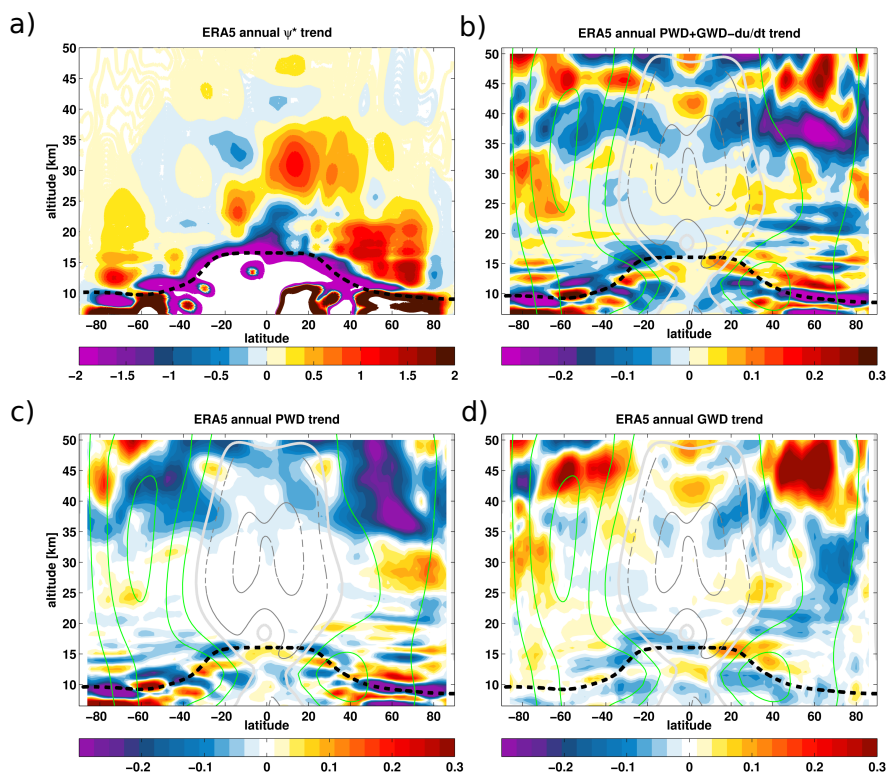
Figure 11. Linear trends of the ψ^* (**a**), net wave forcing (**b**), planetary wave drag (**c**) and gravity wave drag (**d**) from the ERA5 for the 1979–2018 time period. The units of the ψ^* trend and wave drag trend are in $m^{-2} . s^{-1} . decade^{-1}$ and $m . s^{-1} . day^{-1} . decade^{-1}$, respectively. The climatological tropopause from the ERA5 is indicated as the black dashed horizontal line.

ERA-Interim and absent in other reanalyses (Abalos et al., 2015; Miyazaki et al., 2016). As a basis for verification, we also calculated the long-term trend in $\overline{w^*}$ in ERA5. This estimated mean upwelling mass flux trend from the ERA5 reanalysis is about 0.1×10^9 kg · s^{-1} · dec^{-1} instead of -0.47 $\times 10^9$ kg · s^{-1} · dec^{-1} for the ERA-Interim. The relative difference between the two reanalyses in the mass flux is not large, but significant and is between 10 % and 20 % below 70 hPa, indicating that the

5   ERA5 upwelling change is more consistent with observed and climate model predicted strengthening BDC than ERA-Interim.
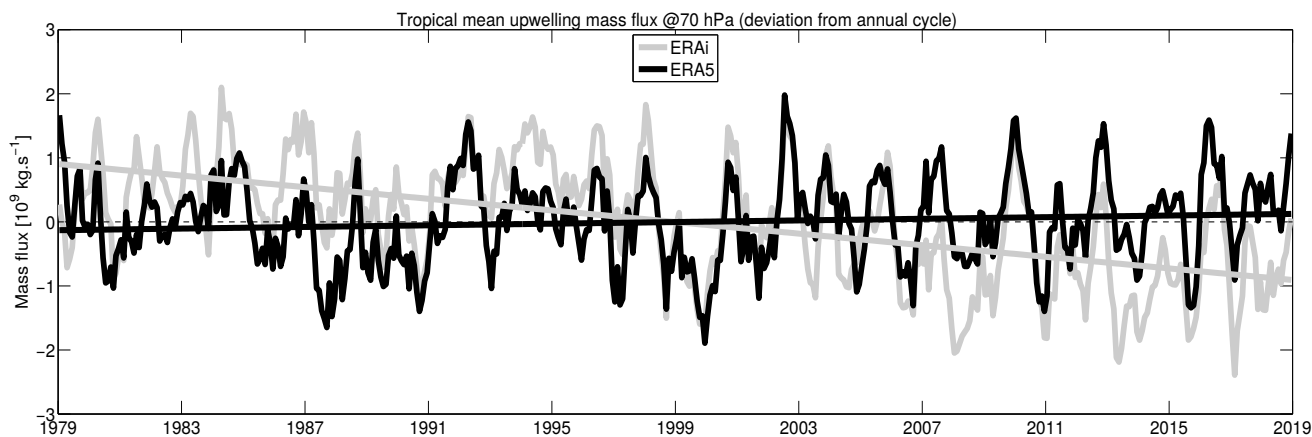
Figure 12. Time series of deseasonalized annual mean tropical upwelling mass flux at 70 hPa ($\sim$19 km) from the ERA5 and the ERA-Interim for the 1979–2018 time period. Shown are ascending flux from the ERA-Interim (Light grey), ascending flux from the ERA5 (Black), trend of the ascending flux from the ERA-Interim (Light grey) and trend of the ascending flux from the ERA5 (Black) for the 1979–2018 time period. The unit of the mass flux is in 10^9 kg . s^{-1}.

5 Summary and Conclusions

In this study, we assess the inter-annual variability and trends of the advective stratospheric BDC in the ERA5 and ERA-Interim reanalyses, using different circulation metrics, including the $\overline{w^*}$, residual stream-function and RCTT. We also evaluate the impact of the natural variability, including the QBO and the ENSO, on the BDC as well as the impact of planetary and
5   gravity wave drag on the BDC and its changes.

Based on our comparisons of the circulation from the ERA5 with the ERA-Interim, we found a remarkably good agreement in the morphology of the advective BDC, including the tropical upwelling and extratropical downwelling as well as in the QBO- and ENSO-induced impact on the BDC. Despite the good agreement in the spatial structure, there are significant differences between the ERA5 and the ERA-Interim in the strength of the advective BDC and in its modulation by the natural variability in the UTLS, and in the upper stratosphere. The advective BDC and its induced-modulations by the natural variability are
10   stronger in ERA5 due to stronger planetary and gravity wave drags. However, in the tropical pipe region below 20 km, the tropical upwelling is about 40 % weaker in ERA5 than in ERA-Interim due to a weaker gravity wave breaking at the equatorial flank of the subtropical jet. In the extra-tropics, the large-scale downwelling is stronger in ERA5 than in ERA-Interim linked to significant differences in planetary and gravity wave drag. These differences in ERA5 vary seasonally and are consistent within all metrics used for evaluating the BDC, including the $\overline{w^*}$, ψ^*, RCTT and modulations by the natural variability. In addition,
15   the differences between the ERA5 and ERA-Interim show a hemispheric asymmetry and a seasonal variation with a maximum difference of about 60 % stronger downwelling in ERA5 arising in the southern hemisphere.

Regarding the QBO signal in the zonal mean wind and temperatures, we found a good agreement in the morphology of the secondary meridional circulation between the two reanalyses. The analysis of the QBO amplitude variation revealed anomalously warm tropical tropopause temperatures associated with the QBO westerly shear modulation, which decreases the tropical upwelling between 15 and 20 km, and also between 30 and 50 km in both reanalyses. Conversely, the QBO easterly shear mod-

5 ulation between 20 and 30 km induced anomalously cold tropical temperatures between 20 and 30 km, leading to enhanced tropical upwelling by the QBO secondary circulation. Besides the good structural agreement, noticeable differences are also found in the strength of the QBO easterly and westerly shear modulations. The QBO modulation is stronger in ERA5 than in ERA-Interim. In the UTLS, the QBO westerly shear in ERA5 is stronger, therefore, consistent with a weaker tropical upwelling in ERA5 compared to ERA-Interim. In addition, the QBO westerly phase in ERA5 extends further down in the UTLS region

10 below the tropical tropopause level.

The regression analysis of the QBO- and ENSO-induced structural changes in $\overline{w^*}$ and ψ^* shows a very good agreement in the modulations of the BDC between the two reanalyses. Similarly to the QBO-induced secondary meridional circulation in the temperatures, both reanalyses agree remarkably well on a weaker upwelling in the UTLS region below 20 km and in the upper stratosphere above 30 km due to the QBO westerly shear and the stronger upwelling in the middle stratosphere induced

15 by the QBO easterly shear. The variations in the residual circulation induced by the ENSO are also very consistent between the two reanalyses. However, significant differences have also been found in the strength of the BDC modulations by the QBO and ENSO. The impact of QBO easterly and westerly shear on the BDC is stronger in ERA5 than in ERA-Interim. Analogously, the ENSO impact on the BDC is globally stronger in ERA5 than in ERA-Interim, except in the UTLS below 20 km where ERA5 seems to be weaker than ERA-Interim, consistent with the weaker ERA5 tropical upwelling.

20 The analysis of the planetary and gravity wave drag clearly shows that the main discrepancies in the BDC in the UTLS region between the ERA5 and ERA-Interim, including the tropical upwelling and mid-latitude downwelling, are mainly due to a weaker gravity wave breaking at the equatorial flank of the subtropical jets in ERA5. The discrepancy in the planetary wave drag between the ERA5 and ERA-Interim is less evident in the UTLS region. In the upper stratosphere above 30 km, the differences in gravity and planetary wave drag between the two reanalyses are significantly large, consistent with a weaker

25 BDC in the UTLS and stronger BDC in the middle and upper stratosphere in ERA5. These differences in wave forcings, therefore, in the BDC strength and its modulations, are very likely related to a combination of several factors, including a higher resolution, higher model top, new non-orographic gravity wave parameterization scheme, and the progress made in the more realistic representation of the sponge layer in ERA5, which is presumably designed to damp upward propagating waves near the model top to avoid reflections from the upper boundary.

30 Finally, the estimates of the advective BDC trend in ERA5 show a global acceleration of the annual mean residual circulation stream-function of about 1.5 % per decade for the 1979-2018 period. Even not statistically significant, this acceleration rate is consistent with observed acceleration of the BDC of about 1.7 % per decade and with future climate model predicted rate of the strength of the BDC of about 2 % per decade due to the increasing level of atmospheric GHGs. The strengthening of the BDC is induced by the increasing planetary and gravity wave breaking in both hemispheres above 30 km. The trends in the

35 residual circulation stream-function are stronger in the northern hemisphere than in the southern hemisphere, consistent with

the trends of the net wave forcing of the BDC. This hemispheric asymmetry in the wave breaking trends is linked to more disturbed winter polar vortex in the northern hemisphere than in the southern hemisphere as well as to ozone recovery in the southern polar vortex (Polvani et al., 2018).

Appendix A: Seasonal variations of planetary and gravity wave forcings
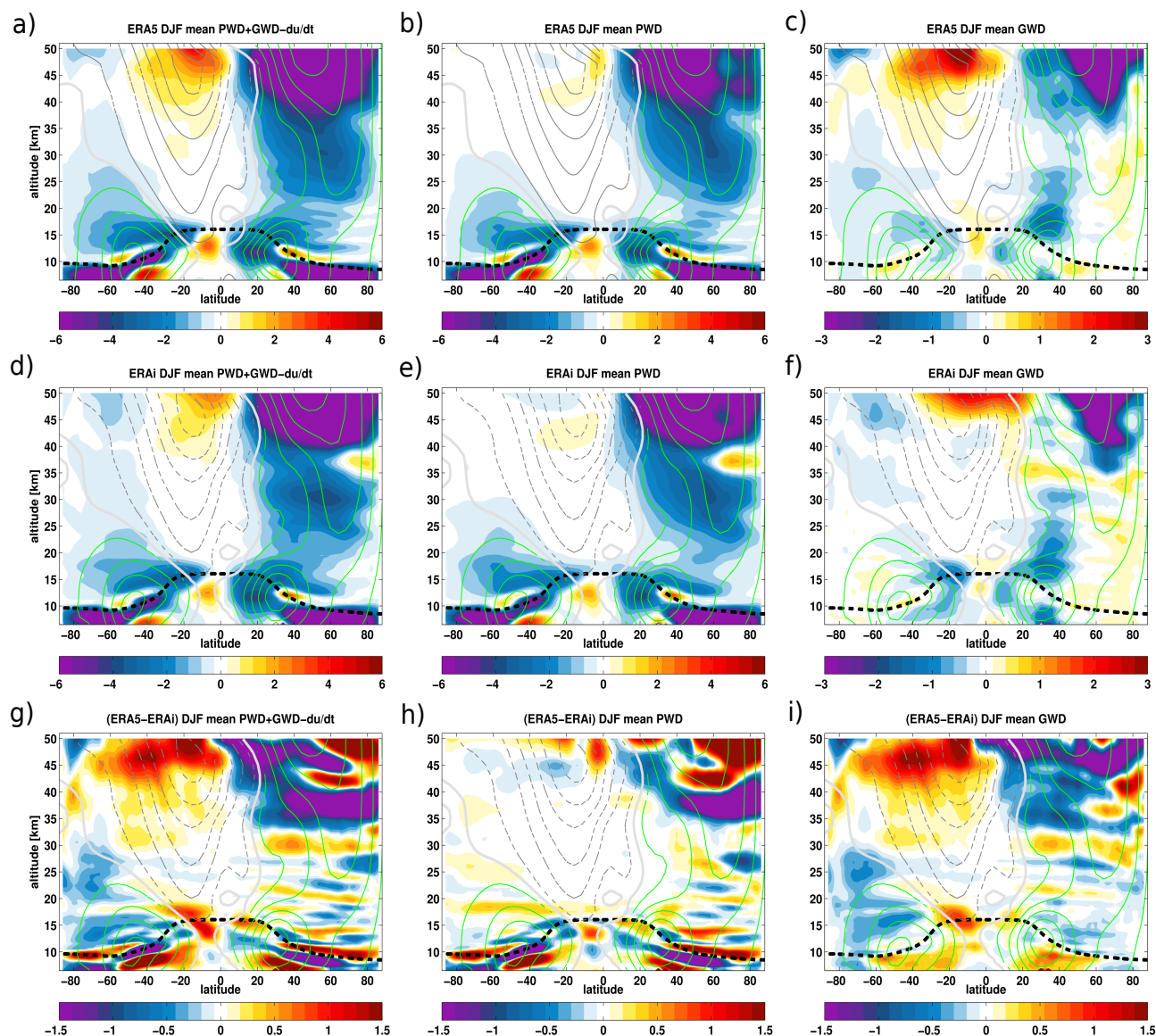
Figure A1. Zonal mean distribution of the winter seasonal mean (DJF) net wave forcing (planetary wave drag + gravity wave drag - du/dt) (**a**, **d**), planetary wave drag (**b**, **e**) and gravity wave drag (**c**, **f**) together with the associated differences (**g-i**) between the ERA5 (**a–c**) and ERA-Interim (**d–f**) for the 1979–2018 time period. The unit of the wave drag is in $m \cdot s^{-1} \cdot day^{-1}$. The climatological tropopause from the ERA-Interim is indicated as the black dashed horizontal line. The thick white line indicates the zero line zonal mean wind. The thin green and grey lines indicate the climatological zonal mean wind.

Data availability. The ERA5 (https://apps.ecmwf.int/data-catalogues/era5/?class=ea last access: 20 August 2020) and ERA-Interim data (https://apps.ecmwf.int/data-catalogues/era-interim/?class=ei, last access: 20 August 2020) are available. The advective BDC and ERA5 data used for this paper may be requested from the corresponding author (m.diallo@fz-juelich.de).
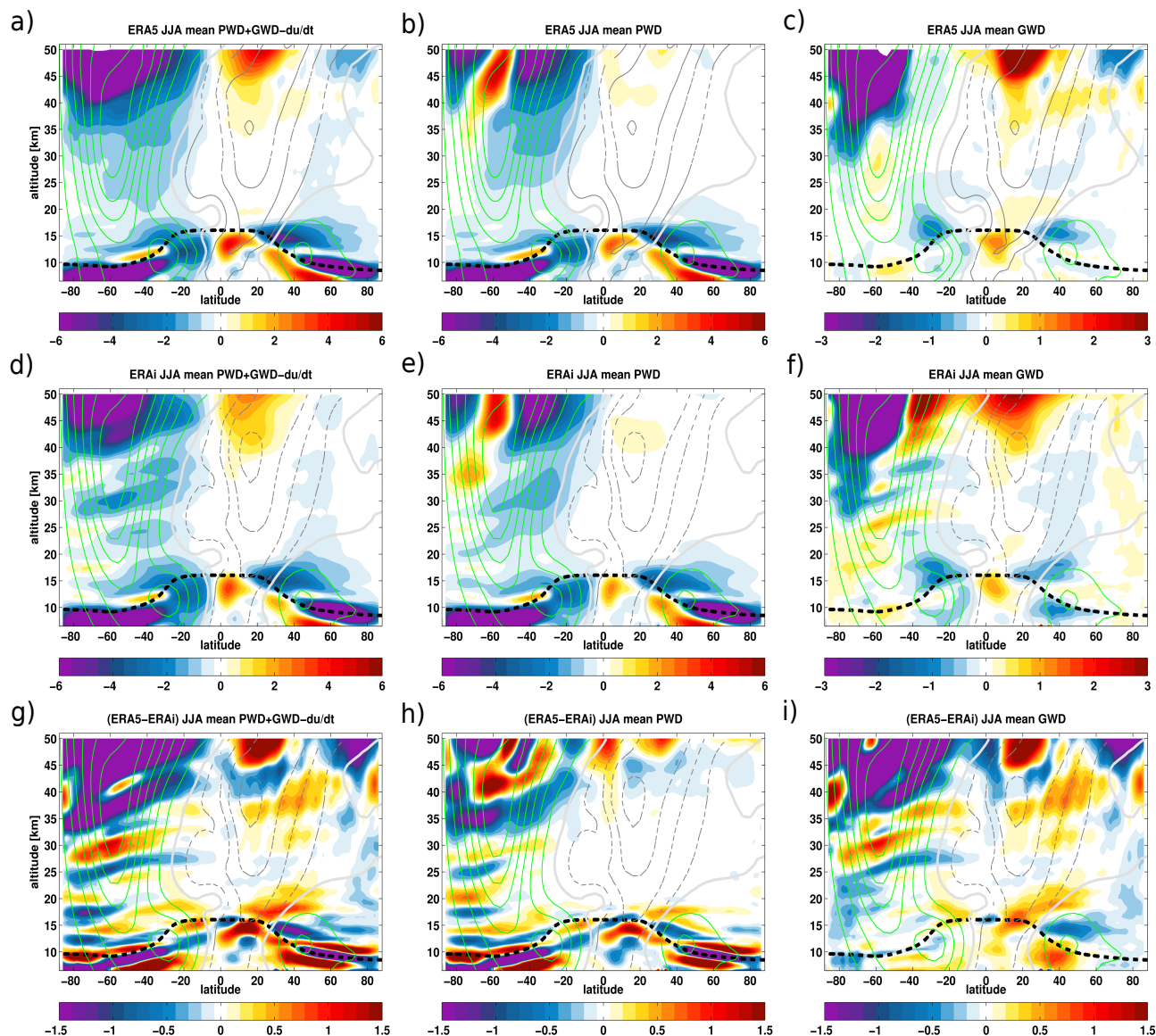
Figure A2. Zonal mean distribution of the summer seasonal mean (JJA) net wave forcing (**a**, **d**), planetary wave drag (**b**, **e**) and gravity wave drag (**c**, **f**), together with the associated differences (**g-i**) between the ERA5 (**a-c**) and ERA-Interim (**d–f**) for the 1979–2018 time period. The The unit of the wave drag is in $m \cdot s^{-1} \cdot day^{-1}$. The climatological tropopause from the ERA-Interim is indicated as the black dashed horizontal line. The thick white line indicates the zero line zonal mean wind. The thin green and grey lines indicate the climatological zonal mean wind.

Author contributions. MD designed the study, conducted research, performed the calculation and the complete analysis of the advective BDC diagnostics as well as drafted the first manuscript. FP calculated the RCTTs. ME calculated the wave decomposition. FP and ME

Atmospheric
Chemistry
and Physics
Discussions

provided helpful discussions and comments. MD edited the final draft with contributions from all co-authors for communication with the journal.

Competing interests. The authors declare that they have no conflict of interest.

Atmospheric
Chemistry
and Physics
Discussions

References

Abalos, M., Legras, B., Ploeger, F., and Randel, W. J.: Evaluating the advective Brewer-Dobson circulation in three reanalyses for the period 1979–2012, J. Geophys. Res. Atmos., 120, 7534–7554, https://doi.org/10.1002/2015JD023182, 2015.

Alexander, M. J. and Rosenlof, K. H.: Nonstationary gravity wave forcing of the stratospheric zonal mean wind, Journal of Geophysical Research: Atmospheres, 101, 23 465–23 474, https://doi.org/10.1029/96JD02197, https://agupubs.onlinelibrary.wiley.com/doi/abs/10.1029/96JD02197, 1996.

Andrews, D. G. and McIntyre, M. E.: Planetary waves in horizontal and vertical shear: the generalized Eliassen-Palm relation and the mean zonal acceleration, J. Atmos. Sci., 33, 2031–2048, 1976.

Andrews, D. G. and McIntyre, M. E.: Generalized Eliassen-Palm and Charney-Dazgin theorems for waves on axisymmetric flows in compressible atmosphere, J. Atmos. Sci., 33, 175–185, 1978.

Andrews, D. G., Holton, J. R., and Leovy, C. B.: Middle Atmosphere Dynamics, vol. 40 of *International Geophysics Series*, Academic Press, San Diego, USA, 1987.

Anstey, J. A., Scinocca, J. F., and Keller, M.: Simulating the QBO in an Atmospheric General Circulation Model: Sensitivity to Resolved and Parameterized Forcing, J. Atmos. Sci., 73, 1649–1665, https://doi.org/10.1175/JAS-D-15-0099.1, https://doi.org/10.1175/JAS-D-15-0099.1, 2016.

Baldwin, M. P. and Dunkerton, T. J.: Stratospheric Harbingers of Anomalous Weather Regimes, Science, 294, 581–584, https://doi.org/10.1126/science.1063315, 2001.

Baldwin, M. P. and O'Sullivan, D.: Stratospheric Effects of ENSO-Related Tropospheric Circulation Anomalies, J. Clim., 8, 649–667, https://doi.org/10.1175/1520-0442(1995)008<0649:SEOERT>2.0.CO;2, 1995.

Baldwin, M. P., Gray, L. J., Dunkerton, T. J., Hamilton, K., Haynes, P. H., Randel, W. J., Holton, J. R., Alexander, M. J., Hirota, I., Horinouchi, T., Jones, D. B. A., Kinnersley, J. S., Marquardt, C., Sato, K., and Takahashi, M.: The quasi-biennial oscillation, Reviews of Geophysics, 39, 179–229, https://doi.org/10.1029/1999RG000073, 2001.

Birner, T. and Bönisch, H. B.: Residual circulation trajectories and transit times into the extratropical lowermost stratosphere, Atmos. Chem. Phys., 11, 817–827, https://doi.org/10.5194/acp-11-817-2011, 2011.

Bjerknes, J.: Atmospheric teleconnections from the equatorial Pacific, Monthly Weather Rev., 97, 163–172, https://doi.org/10.1175/1520-0493(1969)097<0163:ATFTEP>2.3.CO;2, 1969.

Bönisch, H. B., Engel, A., Birner, T., Hoor, P., Tarasick, D. W., and Ray, E. A.: On the structural changes in the Brewer-Dobson circulation after 2000, Atmos. Chem. Phys., 11, 3937–3948, https://doi.org/10.5194/acp-11-3937-2011, 2011.

Brewer, A.: Evidence for a world circulation provided by the measurements of helium and water vapour distribution in the stratosphere, Q. J. R. Meteorol. Soc., 75, 351–363, 1949.

Butchart, N.: The Brewer-Dobson circulation, Rev. of Geophys., 52, 157–184, https://doi.org/10.1002/2013RG000448, http://dx.doi.org/10.1002/2013RG000448, 2014.

Butchart, N., Cionni, I., Eyring, V., Shepherd, T. G., Waugh, D. W., Akiyoshi, H., Austin, J., Brühl, C., Chipperfield, M. P., Cordero, E., Dameris, M., Deckert, R., Dhomse, S., Frith, S. M., Garcia, R. R., Gettelman, A., Giorgetta, M. A., Kinnison, D. E., Li, F., Mancini, E., McLandress, C., Pawson, S., Pitari, G., Plummer, D. A., Rozanov, E., Sassi, F., Scinocca, J. F., Shibata, K., Steil, B., and Tian, W.: Chemistry-Climate Model simulations of twenty-first century stratospheric climate and circulation changes, J. Climate, 23, 5349–5374, https://doi.org/10.1175/2010JCLI3404.1, 2010.

Cagnazzo, C. and Manzini, E.: Impact of the Stratosphere on the Winter Tropospheric Teleconnections between ENSO and the North Atlantic and European Region, J. Clim., 22, 1223–1238, https://doi.org/10.1175/2008JCLI2549.1, 2009.

Cai, W., Borlace, S., Lengaigne, M., van Rensch, P., Collins, M., Vecchi, G., Timmermann, A., Santoso, A., McPhaden, M. J., Wu, L., England, M. H., Wang, G., Guilyardi, E., and Jin, F.-F.: Increasing frequency of extreme El Niño events due to greenhouse warming, Nat. Clim. Change, 4, 111–116, https://doi.org/10.1038/nclimate2100, 2014.

Calvo, N., Garcia, R. R., Randel, W. J., and Marsh, D. R.: Dynamical mechanism for the increase in tropical upwelling in the lowermost tropical stratosphere during warm ENSO events, J. Atmos. Sci., 67, 2331–2340, https://doi.org/10.1175/2010JAS3433.1, 2010.

Chabrillat, S., Vigouroux, C., Christophe, Y., Engel, A., Errera, Q., Minganti, D., Monge-Sanz, B. M., Segers, A., and Mahieu, E.: Comparison of mean age of air in five reanalyses using the BASCOE transport model, Atmos. Chem. Phys., 18, 14 715–14 735, https://doi.org/10.5194/acp-18-14715-2018, https://www.atmos-chem-phys.net/18/14715/2018/, 2018.

Charney, J. G. and Drazin, P. G.: Propagation of planetary-scale disturbances from the lower into upper stratophere, J. Geophys. Res., 66, 83–109, 1961.

Choi, W., Lee, H., Grant, W. B., Park, J. H., Holton, J. R., Lee, K.-M., and Naujokat, B.: On the secondary meridional circulation associated with the quasi-biennial oscillation, Tellus B: Chemical and Physical Meteorology, 54, 395–406, https://doi.org/10.3402/tellusb.v54i4.16673, https://doi.org/10.3402/tellusb.v54i4.16673, 2002.

Collimore, C. C., Martin, D. W., Hitchman, M. H., Huesmann, A., and Waliser, D. E.: On The Relationship between the QBO and Tropical Deep Convection, Journal of Climate, 16, 2552–2568, https://doi.org/10.1175/1520-0442(2003)016<2552:OTRBTQ>2.0.CO;2, https://doi.org/10.1175/1520-0442(2003)016<2552:OTRBTQ>2.0.CO;2, 2003.

Dee, D. P., Uppala, S. M., Simmons, A. J., Berrisford, P., Poli, P., Kobayashi, S., Andrae, U., Balmaseda, M. A., Balsamo, G., Bauer, P., Bechtold, P., Beljaars, A. C. M., van de Berg, L., Bidlot, J., Bormann, N., Delsol, C., Dragani, R., Fuentes, M., Geer, A. J., Haimberger, L., Healy, S. B., Hersbach, H., Hólm, E. V., Isaksen, L., Kållberg, P., Köhler, M., Matricardi, M., McNally, A. P., Monge-Sanz, B. M., Morcrette, J.-J., Park, B.-K., Peubey, C., de Rosnay, P., Tavolato, C., Thépaut, J.-N., and Vitart, F.: The ERA-Interim reanalysis: configuration and performance of the data assimilation system, Q. J. R. Meteorol. Soc., 137, 553–597, https://doi.org/10.1002/qj.828, 2011.

Diallo, M., Legras, B., and Chédin, A.: Age of stratospheric air in the ERA-Interim, Atmos. Chem. Phys., 12, 12 133–12 154, https://doi.org/10.5194/acp-12-12133-2012, 2012.

Diallo, M., Ploeger, F., Konopka, P., Birner, T., Müller, R., Riese, M., Garny, H., Legras, B., Ray, E., Berthet, G., and Jegou, F.: Significant Contributions of Volcanic Aerosols to Decadal Changes in the Stratospheric Circulation, Geophysical Research Letters, 44, 10,780–10,791, https://doi.org/10.1002/2017GL074662, https://agupubs.onlinelibrary.wiley.com/doi/abs/10.1002/2017GL074662, 2017.

Diallo, M., Riese, M., Birner, T., Konopka, P., Müller, R., Hegglin, M. I., Santee, M. L., Baldwin, M., Legras, B., and Ploeger, F.: Response of stratospheric water vapor and ozone to the unusual timing of El Niño and the QBO disruption in 2015–2016, Atmospheric Chemistry and Physics, 18, 13 055–13 073, https://doi.org/10.5194/acp-18-13055-2018, https://www.atmos-chem-phys.net/18/13055/2018/, 2018.

Diallo, M., Konopka, P., Santee, M. L., Müller, R., Tao, M., Walker, K. A., Legras, B., Riese, M., Ern, M., and Ploeger, F.: Structural changes in the shallow and transition branch of the Brewer–Dobson circulation induced by El Niño, Atmospheric Chemistry and Physics, 19, 425–446, https://doi.org/10.5194/acp-19-425-2019, https://www.atmos-chem-phys.net/19/425/2019/, 2019.

Dietmüller, S., Garny, H., Plöger, F., Jöckel, P., and Cai, D.: Effects of mixing on resolved and unresolved scales on stratospheric age of air, Atmospheric Chemistry and Physics, 17, 7703–7719, https://doi.org/10.5194/acp-17-7703-2017, https://www.atmos-chem-phys.net/17/7703/2017/, 2017.

Atmospheric
Chemistry
and Physics
Discussions
Open Access
EGU

Dunkerton, T. J., Hsu, C.-P., and McIntyre, M. E.: On the mean meridional mass motions of the stratosphere and mesosphere, J. Atmos. Sci., 35, 2325–2333, 1978.

Dunkerton, T. J., Hsu, C.-P., and McIntyre, M. E.: Some Eulerian and Lagrangian diagnostics for a model stratospheric warming, J. Atmos. Sci., 38, 819–843, 1981.

5 Eichinger, R., Dietmüller, S., Garny, H., Šácha, P., Birner, T., Bönisch, H., Pitari, G., Visioni, D., Stenke, A., Rozanov, E., Revell, L., Plummer, D. A., Jöckel, P., Oman, L., Deushi, M., Kinnison, D. E., Garcia, R., Morgenstern, O., Zeng, G., Stone, K. A., and Schofield, R.: The influence of mixing on the stratospheric age of air changes in the 21st century, Atmospheric Chemistry and Physics, 19, 921–940, https://doi.org/10.5194/acp-19-921-2019, https://www.atmos-chem-phys.net/19/921/2019/, 2019.

Eichinger, R., Garny, H., Šácha, P., Danker, J., Dietmüller, S., and Oberländer-Hayn, S.: Effects of missing gravity waves on stratospheric
10 dynamics; part 1: climatology, Climate Dynamics, 54, 3165–3183, https://doi.org/https://doi.org/10.1007/s00382-020-05166-w, https://doi.org/10.1007/s00382-020-05166-w, 2020.

Eliassen, A. and Palm, E.: On the transfer of energy in stationary mountain waves, Geofy. Publ., 22, 1–23, 1961.

Engel, A., Bönisch, H., Ullrich, M., Sitals, R., Membrive, O., Danis, F., and Crevoisier, C.: Mean age of stratospheric air derived from AirCore observations, Atmospheric Chemistry and Physics, 17, 6825–6838, https://doi.org/10.5194/acp-17-6825-2017, https://www.
15 atmos-chem-phys.net/17/6825/2017/, 2017.

Ern, M. and Preusse, P.: Wave fluxes of equatorial Kelvin waves and QBO zonal wind forcing derived from SABER and ECMWF temperature space-time spectra, Atmos. Chem. Phys., 9, 3957–3986, https://doi.org/10.5194/acp-9-3957-2009, 2009.

Ern, M., Ploeger, F., Preusse, P., Gille, J. C., Gray, L. J., Kalisch, S., Mlynczak, M. G., Russell, J. M., and Riese, M.: Interaction of gravity waves with the QBO: A satellite perspective, J. Geophys. Res.: Atmospheres, 119, 2329–2355, https://doi.org/10.1002/2013JD020731,
20 2014.

Ern, M., Preusse, P., and Riese, M.: Driving of the SAO by gravity waves as observed from satellite, Ann. Geophys., 33, 483–504, https://doi.org/10.5194/angeo-33-483-2015, 2015.

Ern, M., Trinh, Q. T., Kaufmann, M., Krisch, I., Preusse, P., Ungermann, J., Zhu, Y., Gille, J. C., Mlynczak, M. G., Russell III, J. M., Schwartz, M. J., and Riese, M.: Satellite observations of middle atmosphere gravity wave absolute momentum flux and of its vertical
25 gradient during recent stratospheric warmings, Atmos. Chem. Phys., 16, 9983–10 019, https://doi.org/10.5194/acp-16-9983-2016, 2016.

Forster, P. M. D. F. and Shine, K. P.: Radiative forcing and temperature trends from stratospheric ozone changes, Geophys. Res. Lett., 102, 10 841–10 855, https://doi.org/10.1029/96JD03510, 1997.

Friston, K., Ashburner, J., Kiebel, S. J., Nichols, T. E., and Penny, W. D., eds.: Statistical Parametric Mapping: The Analysis of Functional Brain Images, Academic Press, http://store.elsevier.com/product.jsp?isbn=9780123725608, 2007.

30 Fu, Q., Solomon, S., Pahlavan, H. A., and Lin, P.: Observed changes in Brewer–Dobson circulation for 1980–2018, Environmental Research Letters, 14, 114 026, https://doi.org/10.1088/1748-9326/ab4de7, https://doi.org/10.1088%2F1748-9326%2Fab4de7, 2019.

Garcia, R. R. and Boville, B. A.: "Downward Control" of the Mean Meridional Circulation and Temperature Distribution of the Polar Winter Stratosphere, Journal of the Atmospheric Sciences, 51, 2238–2245, https://doi.org/10.1175/1520-0469(1994)051<2238:COTMMC>2.0.CO;2, https://doi.org/10.1175/1520-0469(1994)051<2238:COTMMC>2.0.CO;2, 1994.

35 Garfinkel, C. I., Shaw, T. A., Hartmann, D. L., and Waugh, D. W.: Does the Holton–Tan Mechanism Explain How the Quasi-Biennial Oscillation Modulates the Arctic Polar Vortex?, Journal of the Atmospheric Sciences, 69, 1713–1733, https://doi.org/10.1175/JAS-D-11-0209.1, https://doi.org/10.1175/JAS-D-11-0209.1, 2012.

Garfinkel, C. I., Aquila, V., Waugh, D. W., and Oman, L. D.: Time-varying changes in the simulated structure of the Brewer–Dobson Circulation, Atmos. Chem. Phys., 17, 1313–1327, https://doi.org/10.5194/acp-17-1313-2017, 2017.

Garny, H., Dameris, M., Randel, W., Bodeker, G. E., and Deckert, R.: Dynamically forced increase of tropical upwelling in the lower stratosphere, J. Atmos. Sci., 68, 1214–1233, https://doi.org/10.1175/2011JAS3701.1, 2011.

Garny, H., Birner, T., Bönisch, H., and Bunzel, F.: The effects of mixing on age of air, J. Geophys. Res. Atmos., 119, https://doi.org/10.1002/2013JD021417, 2014.

Geller, M. A., Zhou, T., Shindell, D., Ruedy, R., Aleinov, I., Nazarenko, L., Tausnev, N. L., Kelley, M., Sun, S., Cheng, Y., Field, R. D., and Faluvegi, G.: Modeling the QBO—Improvements resulting from higher-model vertical resolution, Journal of Advances in Modeling Earth Systems, 8, 1092–1105, https://doi.org/10.1002/2016MS000699, https://agupubs.onlinelibrary.wiley.com/doi/abs/10.1002/2016MS000699, 2016.

Haenel, F. J., Stiller, G. P., von Clarmann, T., Funke, B., Eckert, E., Glatthor, N., Grabowski, U., Kellmann, S., Kiefer, M., Linden, A., and Reddmann, T.: Reassessment of MIPAS age of air trends and variability, Atmos. Chem. and Phys., 15, 13 161–13 176, https://doi.org/10.5194/acp-15-13161-2015, http://www.atmos-chem-phys.net/15/13161/2015/, 2015.

Hardiman, S. C., Butchart, N., and Calvo, N.: The morphology of the Brewer–Dobson circulation and its response to climate change in CMIP5 simulations, Q. J. R. Meteorol. Soc., 140, 1958–1965, https://doi.org/10.1002/qj.2258, 2014.

Haynes, P. H., McIntyre, M. E., Shepherd, T. G., Marks, C. J., and Shine, K. P.: On the "Downward Control" of Extratropical Diabatic Circulations by Eddy-Induced Mean Zonal Forces, J. Atmos. Sci., 48, 651–678, https://doi.org/10.1175/1520-0469(1991)048<0651:OTCOED>2.0.CO;2, 1991.

Hegglin, M. I., Plummer, D. A., Shepherd, T. G., Scinocca, J. F., Anderson, J., Froidevaux, L., Funke, B., Hurst, D., Rozanov, A., Urban, J., von Clarmann, T., Walker, K. A., Wang, H. J., Tegtmeier, S., and Weigel, K.: Vertical structure of stratospheric water vapour trends derived from merged satellite data, Nature Geosci., 7, 768–776, https://doi.org/10.1038/ngeo2236, 2014.

Hersbach, H., Bell, B., Berrisford, P., Hirahara, S., Horányi, A., Muñoz-Sabater, J., Nicolas, J., Peubey, C., Radu, R., Schepers, D., Simmons, A., Soci, C., Abdalla, S., Abellan, X., Balsamo, G., Bechtold, P., Biavati, G., Bidlot, J., Bonavita, M., De Chiara, G., Dahlgren, P., Dee, D., Diamantakis, M., Dragani, R., Flemming, J., Forbes, R., Fuentes, M., Geer, A., Haimberger, L., Healy, S., Hogan, R. J., Hólm, E., Janisková, M., Keeley, S., Laloyaux, P., Lopez, P., Lupu, C., Radnoti, G., de Rosnay, P., Rozum, I., Vamborg, F., Villaume, S., and Thépaut, J.-N.: The ERA5 Global Reanalysis, Q. J. R. Meteorol. Soc., n/a, https://doi.org/10.1002/qj.3803, https://rmets.onlinelibrary.wiley.com/doi/abs/10.1002/qj.3803, 2020.

Hoffmann, L., Günther, G., Li, D., Stein, O., Wu, X., Griessbach, S., Heng, Y., Konopka, P., Müller, R., Vogel, B., and Wright, J. S.: From ERA-Interim to ERA5: the considerable impact of ECMWF's next-generation reanalysis on Lagrangian transport simulations, Atmospheric Chemistry and Physics, 19, 3097–3124, https://doi.org/10.5194/acp-19-3097-2019, https://www.atmos-chem-phys.net/19/3097/2019/, 2019.

Holton, J. R.: On the global exchange of mass between the stratosphere and troposphere, J. Atmos. Sci., 47, 651–678, 1990.

Holton, J. R. and Lindzen, R. S.: An Updated Theory for the Quasi-Biennial Cycle of the Tropical Stratosphere, Journal of the Atmospheric Sciences, 29, 1076–1080, https://doi.org/10.1175/1520-0469(1972)029<1076:AUTFTQ>2.0.CO;2, https://doi.org/10.1175/1520-0469(1972)029<1076:AUTFTQ>2.0.CO;2, 1972.

Holton, J. R. and Tan, H.-C.: The Influence of the Equatorial Quasi-Biennial Oscillation on the Global Circulation at 50 mb, Journal of the Atmospheric Sciences, 37, 2200–2208, https://doi.org/10.1175/1520-0469(1980)037<2200:TIOTEQ>2.0.CO;2, https://doi.org/10.1175/1520-0469(1980)037<2200:TIOTEQ>2.0.CO;2, 1980.

Holton, J. R., Haynes, P. H., McIntyre, M. E., Douglass, A. R., Rood, R. B., and Pfister, L.: Stratosphere-troposphere exchange, Rev. Geophys., 33, 403–440, https://doi.org/10.1029/95RG02097, 1995.

Kawatani, Y. and Hamilton, K.: Weakened stratospheric quasibiennial oscillation driven by increased tropical mean upwelling, Nature, 497, 478–481, https://doi.org/doi:10.1038/nature12140, 2013.

5 Konopka, P., Ploeger, F., Tao, M., and Riese, M.: Zonally resolved impact of ENSO on the stratospheric circulation and water vapor entry values, J. Geophys. Res.: Atmospheres, 121, 11,486–11,501, https://doi.org/10.1002/2015JD024698, 2016.

Lacis, A. A., Chowdhary, J., Mishchenko, M. I., and Cairns, B.: Modeling errors in diffuse-sky radiation: Vector vs scalar treatment, Geophysical Research Letters, 25, 135–138, https://doi.org/10.1029/97GL03613, https://agupubs.onlinelibrary.wiley.com/doi/abs/10.1029/97GL03613, 1998.

10 Latif, M. and Keenlyside, N. S.: El Niño/Southern Oscillation response to global warming, Proceed. of the Nat. Acad. of Sci., 106, 20 578–20 583, https://doi.org/10.1073/pnas.0710860105, 2009.

Li, D., Vogel, B., Müller, R., Bian, J., Günther, G., Ploeger, F., Li, Q., Zhang, J., Bai, Z., Vömel, H., and Riese, M.: Dehydration and low ozone in the tropopause layer over the Asian monsoon caused by tropical cyclones: Lagrangian transport calculations using ERA-Interim and ERA5 reanalysis data, Atmospheric Chemistry and Physics, 20, 4133–4152, https://doi.org/10.5194/acp-20-4133-2020, https://www.atmos-chem-phys.net/20/4133/2020/, 2020.

15 Li, F., Austin, J., and Wilson, J.: The strength of the Brewer Dobson Circulation in a changing climate: Coupled chemistry climate model simulations, J. Clim., 21, 40, https://doi.org/10.1175/2007JCLI1663.1, 2008.

Lin, P. and Fu, Q.: Changes in various branches of the Brewer–Dobson circulation from an ensemble of chemistry climate models, J. Geophys. Res. Atmos., 118, 73–84, https://doi.org/10.1029/2012JD018813, https://agupubs.onlinelibrary.wiley.com/doi/abs/10.1029/2012JD018813, 2013.

20 Lindzen, R. S. and Fox-Rabinovitz, M.: Consistent Vertical and Horizontal Resolution, Monthly Weather Review, 117, 2575–2583, https://doi.org/10.1175/1520-0493(1989)117<2575:CVAHR>2.0.CO;2, https://doi.org/10.1175/1520-0493(1989)117<2575:CVAHR>2.0.CO;2, 1989.

Lindzen, R. S. and Holton, J. R.: A Theory of the Quasi-Biennial Oscillation, J. Atmos. Sci., 25, 1095–1107, https://doi.org/10.1175/1520-0469(1968)025<1095:ATOTQB>2.0.CO;2, 1968.

25 Linz, M., Plumb, R. A., Gerber, E. P., Haenel, F. J., Stiller, G., Kinnison, D. E., Ming, A., and Neu, J. L.: The strength of the meridional overturning circulation of the stratosphere, Nature Geosci., 10, 663–667, https://doi.org/https://doi.org/10.1038/ngeo3013, 2017.

Lott, F., Guez, L., and Maury, P.: A stochastic parameterization of non-orographic gravity waves: Formalism and impact on the equatorial stratosphere, Geophys. Res. Lett., 39, https://doi.org/10.1029/2012GL051001, https://agupubs.onlinelibrary.wiley.com/doi/abs/10.1029/2012GL051001, 2012.

30 Lu, H., Bracegirdle, T. J., Phillips, T., Bushell, A., and Gray, L.: Mechanisms for the Holton-Tan relationship and its decadal variation, Journal of Geophysical Research: Atmospheres, 119, 2811–2830, https://doi.org/10.1002/2013JD021352, https://agupubs.onlinelibrary.wiley.com/doi/abs/10.1002/2013JD021352, 2014.

McIntyre, M. E. and Palmer, T. N.: The surf zone in the stratosphere, J. Atmos. Terr. Phys., 46, 825–849, https://doi.org/https://doi.org/10.1016/0021-9169(84)90063-1, 1984.

35 McLandress, C. and Shepherd, T. G.: Simulated anthropogenic changes in the Brewer-Dobson Circulation, Including Its Extension to High Latitudes, J. Clim., 22, 1516, https://doi.org/10.1175/2008JCLI2679.1, 2009.

McLandress, C., Shepherd, T. G., Polavarapu, S., and Beagley, S. R.: Is Missing Orographic Gravity Wave Drag near 60°S the Cause of the Stratospheric Zonal Wind Biases in Chemistry–Climate Models?, J. Atmos. Sci., 69, 802–818, https://doi.org/10.1175/JAS-D-11-0159.1, https://doi.org/10.1175/JAS-D-11-0159.1, 2012.

Miyazaki, K., Iwasaki, T., Kawatani, Y., Kobayashi, C., Sugawara, S., and Hegglin, M. I.: Inter-comparison of stratospheric mean-meridional circulation and eddy mixing among six reanalysis data sets, Atmospheric Chemistry and Physics, 16, 6131–6152, https://doi.org/10.5194/acp-16-6131-2016, https://www.atmos-chem-phys.net/16/6131/2016/, 2016.

Monge-Sanz, B. M., Chipperfield, M. P., Dee, D. P., Simmons, A. J., and Uppala, S. M.: Improvements in the stratospheric transport achieved by a chemistry transport model with ECMWF (re)analyses: identifying effects and remaining challenges, https://doi.org/10.1002/qj.1996, 2012.

Neu, J. L. and Plumb, R. A.: Age of air in a "leaky pipe" model of stratospheric transport, J. Geophys. Res., 104, 19,243–19,255, https://doi.org/10.1029/1999JD900251, 1999.

Newman, P. A. and Nash, E. R.: Quantifying the wave driving of the stratosphere, J. Geophys. Res.: Atmospheres, 105, 12 485–12 497, https://doi.org/10.1029/1999JD901191, 2000.

Newman, P. A., Coy, L., Pawson, S., and Lait, L. R.: The anomalous change in the QBO in 2015–2016, Geophys. Res. Lett., 43, 8791–8797, https://doi.org/10.1002/2016GL070373, 2016.

Niwano, M., Yamazaki, K., and Shiotani, M.: Seasonal and QBO variations of ascent rate in the tropical lower stratosphere as inferred from UARS HALOE trace gas data, J. Geophys. Res., 108, 4794, https://doi.org/10.1029/2003JD003871, 4794, 2003.

Orr, A., Bechtold, P., Scinocca, J., Ern, M., and Janiskova, M.: Improved middle atmosphere climate and forecasts in the ECMWF model through a non-orographic gravity wave drag parametrization, https://www.ecmwf.int/node/16955, 2010.

Osprey, S. M., Butchart, N., Knight, J. R., Scaife, A. A., Hamilton, K., Anstey, J. A., Schenzinger, V., and Zhang, C.: An unexpected disruption of the atmospheric quasi-biennial oscillation, Science, https://doi.org/10.1126/science.aah4156, 2016.

Philander, S. G.: El Niño, La Nina, and the Southern Oscillation, vol. 46 of *Academic Press*, Cambridge Univ. Press, San Diego, CA, 1990.

Ploeger, F., Konopka, P., Müller, R., Fueglistaler, S., Schmidt, T., Manners, J. C., Grooβ, J.-U., Günther, G., Forster, P. M., and Riese, M.: Horizontal transport affecting trace gas seasonality in the Tropical Tropopause Layer (TTL), J. Geophys. Res., 117, https://doi.org/10.1029/2011JD017267, 2012.

Ploeger, F., Abalos, M., Birner, T., Konopka, P., Legras, B., Müller, R., and Riese, M.: Quantifying the effects of mixing and residual circulation on trends of stratospheric mean age of air, Geophys. Res. Lett., 42, https://doi.org/10.1002/2014GL062927, 2015a.

Ploeger, F., Riese, M., Haenel, F., Konopka, P., Müller, R., and Stiller, G.: Variability of stratospheric mean age of air and of the local effects of residual circulation and eddy mixing, J. Geophys. Res. Atmos., 120, https://doi.org/10.1002/2014JD022468, 2015b.

Ploeger, F., Legras, B., Charlesworth, E., Yan, X., Diallo, M., Konopka, P., Birner, T., Tao, M., Engel, A., and Riese, M.: How robust are stratospheric age of air trends from different reanalyses?, Atmos. Chem. Phys., 19, 6085–6105, https://doi.org/10.5194/acp-19-6085-2019, https://www.atmos-chem-phys.net/19/6085/2019/, 2019.

Plumb, R. A.: The Interaction of Two Internal Waves with the Mean Flow: Implications for the Theory of the Quasi-Biennial Oscillation, Journal of the Atmospheric Sciences, 34, 1847–1858, https://doi.org/10.1175/1520-0469(1977)034<1847:TIOTIW>2.0.CO;2, https://doi.org/10.1175/1520-0469(1977)034<1847:TIOTIW>2.0.CO;2, 1977.

Plumb, R. A.: Stratospheric transport, J. Meteor. Soc. Japan, 80, 793–809, 2002.

Plumb, R. A. and Bell, R. C.: A model of the quasi-biennial oscillation on an equatorial beta-plane, Q. J. R. Meteorol. Soc., 108, 335–352, https://doi.org/10.1002/qj.49710845604, 1982.

Plumb, R. A. and Eluszkiewicz, P.: he Brewer-Dobson circulation: dynamics of the tropical upwelling, J. Atmos. Sci., 56, 868–890, 1999.

Polichtchouk, I., Hogan, R., Shepherd, T. G., Bechtold, P., Stockdale, T., Malardel, S., Lock, S.-J., and Magnusson, L.: What influences the middle atmosphere circulation in the IFS?, https://doi.org/10.21957/mfsnfv15o, https://www.ecmwf.int/node/17670, 2017.

Polichtchouk, I., Shepherd, T. G., Hogan, R. J., and Bechtold, P.: Sensitivity of the Brewer–Dobson Circulation and Polar Vortex Variability to Parameterized Nonorographic Gravity Wave Drag in a High-Resolution Atmospheric Model, Journal of the Atmospheric Sciences, 75, 1525–1543, https://doi.org/10.1175/JAS-D-17-0304.1, https://doi.org/10.1175/JAS-D-17-0304.1, 2018.

Polvani, L. M., Abalos, M., Garcia, R., Kinnison, D., and Randel, W. J.: Significant Weakening of Brewer-Dobson Circulation Trends Over the 21st Century as a Consequence of the Montreal Protocol, Geophys. Res. Lett., 45, 401–409, https://doi.org/10.1002/2017GL075345, https://agupubs.onlinelibrary.wiley.com/doi/abs/10.1002/2017GL075345, 2018.

Punge, H. J., Konopka, P., Giorgetta, M. A., and Müller, R.: Effect of the quasi-biennial oscillation on low-latitude transport in the stratosphere derived from trajectory calculations, J. Geophys. Res., 114, D03 102, https://doi.org/10.1029/2008JD010518, 2009.

Randel, W.: Ideas flow on Antarctic polar vortex, Nature, 364, 105–106, 1993.

Randel, W. J., Garcia, R. R., and Wu, F.: Time-Dependent Upwelling in the Tropical Lower Stratosphere Estimated from the Zonal-Mean Momentum Budget, Journal of the Atmospheric Sciences, 59, 2141–2152, https://doi.org/10.1175/1520-0469(2002)059<2141:TDUITT>2.0.CO;2, https://doi.org/10.1175/1520-0469(2002)059<2141:TDUITT>2.0.CO;2, 2002.

Randel, W. J., Wu, F., Vömel, H., Nedoluha, G. E., and Forster, P.: Decreases in stratospheric water vapor after 2001: Links to changes in the tropical tropopause and the Brewer-Dobson circulation, J. Geophys. Res., 111, 12 312, https://doi.org/10.1029/2005JD006744, d12312, 2006.

Randel, W. J., Garcia, R., and Wu, F.: Dynamical Balances and Tropical Stratospheric Upwelling, Journal of the Atmospheric Sciences, 65, 3584–3595, https://doi.org/10.1175/2008JAS2756.1, https://doi.org/10.1175/2008JAS2756.1, 2008.

Randel, W. J., Garcia, R. R., Calvo, N., and Marsh, D.: ENSO influence on zonal mean temperature and ozone in the tropical lower stratosphere, Geophys. Res. Lett., 39, https://doi.org/10.1029/2009GL039343, 2009.

Ray, E. A., Moore, F. L., Rosenlof, K. H., Davis, S. M., Boenisch, H., Morgenstern, O., Smale, D., Rozanov, E., Hegglin, M., Pitari, G., Mancini, E., Braesicke, P., Butchart, N., Hardiman, S., Li, F., Shibata, K., and Plummer, D. A.: Evidence for changes in stratospheric transport and mixing over the past three decades based on multiple data sets and tropical leaky pipe analysis, J. Geophys. Res., 115, https://doi.org/10.1129/2010JD014206, 2010.

Ray, E. A., Moore, F. L., Rosenlof, K. H., Davis, S. M., Sweeney, C., Bönisch, H., Engel, A., Sugawara, S., Nakazawa, T., and Aoki, S.: Improving stratospheric transport trend analysis based on SF6 and CO2 measurements, J. Geophys. Res., 119, 14 110–14 128, https://doi.org/10.1002/2014JD021802, 2014.

Ray, E. A., Portmann, R. W., Yu, P. e. a., Daniel, J., Montzka, S. A., Dutton, G. S., Hall, B. D., Moore, F. L., and Rosenlof, K. H.: The influence of the stratospheric Quasi-Biennial Oscillation on trace gas levels at the Earth's surface, Nat. Geosci., 13, 22–27, https://doi.org/https://doi.org/10.1038/s41561-019-0507-3, 2020.

Richter, J. H., Solomon, A., and Bacmeister, J. T.: On the simulation of the quasi-biennial oscillation in the Community Atmosphere Model, version 5, Journal of Geophysical Research: Atmospheres, 119, 3045–3062, https://doi.org/10.1002/2013JD021122, https://agupubs.onlinelibrary.wiley.com/doi/abs/10.1002/2013JD021122, 2014.

Riese, M., Ploeger, F., Rap, A., Vogel, B., Konopka, P., Dameris, M., and Forster, P.: Impact of uncertainties in atmospheric mixing on simulated UTLS composition and related radiative effects, J. Geophys. Res., 117, D16305, https://doi.org/10.1029/2012JD017751, 2012.

Rosenlof, K. and Holton, J.: Estimates of the stratospheric residual circulation using the downward control principle, J. Geophys. Res., 98, 10,465–10,479, 1993.

Saravanan, R.: A Multiwave Model of the Quasi-biennial Oscillation, J. Atmos. Sci., 47, 2465–2474, https://doi.org/10.1175/1520-0469(1990)047<2465:AMMOTQ>2.0.CO;2, 1990.

Scaife, A. A., Butchart, N., Warner, C. D., and Swinbank, R.: Impact of a Spectral Gravity Wave Parameterization on the Stratosphere in the Met Office Unified Model, J. Atmos. Sci., 59, 1473–1489, https://doi.org/10.1175/1520-0469(2002)059<1473:IOASGW>2.0.CO;2, https://doi.org/10.1175/1520-0469(2002)059<1473:IOASGW>2.0.CO;2, 2002.

Seviour, W. J. M., Butchart, N., and Hardiman, S. C.: The Brewer–Dobson circulation inferred from ERA-Interim, Q. J. R. Meteorol. Soc., pp. n/a–n/a, https://doi.org/10.1002/qj.966, http://dx.doi.org/10.1002/qj.966, 2011.

Shepherd, T., Polichtchouk, I., Hogan, R., and Simmons, A. J.: Report on Stratosphere Task Force, https://doi.org/10.21957/0vkp0t1xx, https://www.ecmwf.int/node/18259, 2018.

Shepherd, T. G.: Transport in the Middle Atmosphere, J. Meteorol. Soc. of Japan. Ser. II, 85B, 165–191, https://doi.org/10.2151/jmsj.85B.165, 2007.

Shepherd, T. G. and McLandress, C.: A Robust Mechanism for Strengthening of the Brewer–Dobson Circulation in Response to Climate Change: Critical-Layer Control of Subtropical Wave Breaking, J. Atmos. Sci., 68, 784–797, https://doi.org/10.1175/2010JAS3608.1, https://doi.org/10.1175/2010JAS3608.1, 2011.

Shuckburgh, E. and Haynes, P. H.: Diagnosed transport and mixing using a tracer-based coordinate system, Phys. Fluids, 15, 3342–3357, https://doi.org/10.1063/1.1610471, 2003.

Sigmond, M. and Shepherd, T. G.: Compensation between Resolved Wave Driving and Parameterized Orographic Gravity Wave Driving of the Brewer–Dobson Circulation and Its Response to Climate Change, Journal of Climate, 27, 5601–5610, https://doi.org/10.1175/JCLI-D-13-00644.1, https://doi.org/10.1175/JCLI-D-13-00644.1, 2014.

Simmons, A., Soci, C., Nicolas, J., Bell, B., Berrisford, P., Dragani, R., Flemming, J., Haimberger, L., Healy, S., Hersbach, H., Horányi, A., Inness, A., Munoz-Sabater, J., Radu, R., and Schepers, D.: Global stratospheric temperature bias and other stratospheric aspects of ERA5 and ERA5.1, https://doi.org/10.21957/rcxqfmg0, https://www.ecmwf.int/node/19362, 2020.

Stiller, G. P., von Clarmann, T., Haenel, F., Funke, B., Glatthor, N., Grabowski, U., Kellmann, S., Kiefer, M., Linden, A., Lossow, S., and López-Puertas, M.: Observed temporal evolution of global mean age of stratospheric air for the 2002 to 2010 period, Atmos. Chem. Phys., 12, 3311–3331, https://doi.org/10.5194/acp-12-3311-2012, http://www.atmos-chem-phys.net/12/3311/2012/, 2012.

Tao, M., Konopka, P., Ploeger, F., Yan, X., Wright, J. S., Diallo, M., Fueglistaler, S., and Riese, M.: Multitimescale variations in modeled stratospheric water vapor derived from three modern reanalysis products, Atmos. Chem. Phys., 19, 6509–6534, https://doi.org/10.5194/acp-19-6509-2019, https://acp.copernicus.org/articles/19/6509/2019/, 2019.

Tegtmeier, S., Anstey, J., Davis, S., Dragani, R., Harada, Y., Ivanciu, I., Pilch Kedzierski, R., Krüger, K., Legras, B., Long, C., Wang, J. S., Wargan, K., and Wright, J. S.: Temperature and tropopause characteristics from reanalyses data in the tropical tropopause layer, Atmos. Chem. Phys., 20, 753–770, https://doi.org/10.5194/acp-20-753-2020, https://www.atmos-chem-phys.net/20/753/2020/, 2020.

Thompson, D. W. J. and Solomon, S.: Recent stratospheric climat trends as evidence inradiosonde data: Global structure and tropospheric linkages., J. Climate, 18, 4785–4795, https://doi.org/10.1175/JCLI3585.1, 2005.

Thompson, D. W. J. and Solomon, S.: Understanding recent stratospheric climate change, J. Climate, 22, 1934, https://doi.org/10.1175/2008JCLI2482.1, 2009.

Trepte, C. R. and Hitchman, M. H.: Tropical stratospheric circulation deduced from satellite aerosol data, Nat. Geosci., 355, 626–628, https://doi.org/10.1038/355626a0, 1992.

van Oldenborgh, G. J., Philip, S. Y., and Collins, M.: El Niño in a changing climate: a multi-model study, Ocean Science, 1, 81–95, https://doi.org/10.5194/os-1-81-2005, 2005.

5 Šácha, P., Eichinger, R., Garny, H., Pišoft, P., Dietmüller, S., de la Torre, L., Plummer, D. A., Jöckel, P., Morgenstern, O., Zeng, G., Butchart, N., and Añel, J. A.: Extratropical age of air trends and causative factors in climate projection simulations, Atmos. Chem. Phys., 19, 7627–7647, https://doi.org/10.5194/acp-19-7627-2019, https://www.atmos-chem-phys.net/19/7627/2019/, 2019.

Wallace, J. M., Panetta, R. L., and Estberg, J.: Representation of the Equatorial Stratospheric Quasi-Biennial Oscillation in EOF Phase Space, J. Atmos. Sci., 50, 1751–1762, https://doi.org/10.1175/1520-0469(1993)050<1751:ROTESQ>2.0.CO;2, 1993.

10 Wang, C., Deser, Y. J.-Y., DiNezio, P., and Clement, A.: El Niño–Southern Oscillation (ENSO): A review. In Reefs of the Eastern Pacific, Springer Sci. Publish., pp. 85–106, 2016.

Warner, C. D. and McIntyre, M. E.: An Ultrasimple Spectral Parameterization for Nonorographic Gravity Waves, J. Atmos. Sci., 58, 1837–1857, https://doi.org/10.1175/1520-0469(2001)058<1837:AUSPFN>2.0.CO;2, https://doi.org/10.1175/1520-0469(2001)058<1837:AUSPFN>2.0.CO;2, 2001.

15 Waugh, D. and Hall, T.: Age of stratospheric air: Theory, observations, and models, Rev. Geophys., 40, 1010, https://doi.org/10.1029/2000RG000101, 2002.

WMO: Scientific Assessment of Ozone Depletion: 2018, Global ozone research and monitoring project - report no. 58, WMO (World Meteorological Organization), Geneva, Switzerland, 2018.

Wolter, K. and Timlin, M. S.: El Nino/Southern Oscillation behaviour since 1871 as diagnosed in an extended multivariate ENSO index 20 (MEI.ext), Int. J. Climatol., 31, 1074–1087, https://doi.org/10.1002/joc.2336, 2011.

Yang, H., Chen, G., and Domeisen, D. I. V.: Sensitivities of the Lower-Stratospheric Transport and Mixing to Tropical SST Heating, Journal of the Atmospheric Sciences, 71, 2674–2694, https://doi.org/10.1175/JAS-D-13-0276.1, https://doi.org/10.1175/JAS-D-13-0276.1, 2014.

Zwiers, F. W. and von Storch, H.: Taking Serial Correlation into Account in Tests of the Mean, J. Clim., 8, 336–351, https://doi.org/10.1175/1520-0442(1995)008<0336:TSCIAI>2.0.CO;2, 1995.